International Journal of Engineering Science 154 (2020) 103310

Contents lists available at ScienceDirect

International Journal of Engineering Science

journal homepage: www.elsevier.com/locate/ijengsci

Interphase effect on the effective magneto-electro-elastic properties for three-phase fiber-reinforced composites by a semi-analytical approach

Y. Espinosa-Almeyda[a,b], H. Camacho-Montes[b], J.A. Otero[c,*], R. Rodríguez-Ramos[d,e], J.C. López-Realpozo[d], R. Guinovart-Díaz[d], F.J. Sabina[a]

[a] Instituto de Investigaciones en Matemáticas Aplicadas y en Sistemas, Universidad Nacional Autónoma de México, Apartado Postal 20-126, Alcaldía Álvaro Obregón, CP. 01000 CDMX, México
[b] Instituto de Ingeniería y Tecnología, Universidad Autónoma de Ciudad Juárez, Av. Del Charro 450 Norte Cd. Juárez, Chihuahua, CP. 32310, México
[c] Departamento de Ciencias, Escuela de ingeniería y Ciencias. Tecnológico de Monterrey, Campus Estado de México, Atizapán de Zaragoza, CP 52926, México
[d] Facultad de Matemática y Computación, Universidad de La Habana, San Lázaro y L, Vedado, La Habana, CP. 10400, Cuba
[e] Escuela de Ingeniería y Ciencias, Tecnológico de Monterrey, Campus Puebla Atlixcáyotl 5718, Reserva Territorial Atlixcáyotl, 72453 Puebla, México

ARTICLE INFO

Article history:
Received 15 October 2019
Revised 23 March 2020
Accepted 29 April 2020
Available online xxx

Keywords:
Fiber-reinforced composites
Effective properties
Finite element method
Magneto-electro-elastic coupling
6 mm symmetry point group

ABSTRACT

A semi-analytical approach is proposed to determine the effective magneto-electro-elastic moduli of a fiber-reinforced composite. We especially focus on predicting the effective properties of three-phase periodic composite reinforced with unidirectional, infinitely long and concentric cylindrical fibers with square transversal distribution. The semi-analytical method is developed combining asymptotic homogenization and finite element methods. Asymptotic homogenization method allows the statements of local problems that are solved by finite element method and the associated effective coefficients. Finite element method is implemented via the principle of minimum potential energy. The effect of interphase thickness and the fiber material properties on effective moduli is analyzed. Numerical computations were performed, and an exact agreement is obtained by comparing the semi-analytical approach with asymptotic homogenization method linked to the theory of potential functions of a complex variable.

1. Introduction

Multi-phase magneto-electro-elastic composites have been receiving great attention in the literature due to the wide application field. Y. Cheng et al. report an updated status for magnetoelectric materials applications (Cheng, Peng, Hu, Zhou, & Liu, 2018). As typical cases, it can be mentioned: field sensors (Reis et al., 2017), energy harvester (Naifar, Bradai, Viehweger, Choura, & Kanoun, 2018; Qiu, Chen, Wen, & Li, 2015; Qiu, Tang, Chen, Liu, & Hu, 2017), random access memory

* Corresponding author.
E-mail addresses: yoanhealmeyda1209@gmail.com (Y. Espinosa-Almeyda), hcamacho@uacj.mx (H. Camacho-Montes), j.a.otero@tec.mx (J.A. Otero), reinaldo@matcom.uh.cu (R. Rodríguez-Ramos), jclrealpozo@matcom.uh.cu (J.C. López-Realpozo), guino@matcom.uh.cu (R. Guinovart-Díaz), fjs@mym.iimas.unam.mx (F.J. Sabina).

https://doi.org/10.1016/j.ijengsci.2020.103310

(Kosub et al., 2017; Lee et al., 2017), voltage tunable inductors (Geng, Yan, Priya, & Wang, 2017; Lin et al., 2015), band stop filters (Ciomaga et al., 2016) and tunable resonators (Popov, Zavislyak, & Srinivasan, 2018). This picture that involves a high number of applications shows the current demand for improving magnetoelectric (ME) composite designs.

Homogenization techniques have always been a useful tool to describe the structure-properties relationship of composite materials (Bakhvalov & Panasenko, 1989). In literature, different homogenization implementations can be found, which represent an important advantage, because it allows validations between models by comparing them. Essentially, different mathematical approaches describing the same physical phenomena must provide quite close results. This is an important validation step toward effective properties calculation to better study a wider range of composites. J. A. Otero and colleagues developed a semi-analytical method for computing elastic effective properties of composites with imperfect interfaces (Otero et al., 2013). H. Berger et al. proposed a scheme fully based on the finite element method (FEM) subjected to a set of boundary conditions focused on specific stress-strain, or stress-electric field relations (Berger et al., 2003, 2005).

The effect of phase contact quality on composite properties is an active issue that has been gaining attention during the last years because it can be a structural factor with heavy influence. It is necessary to consider this effect to develop more realistic property estimations. D. Guinovart-Sanjuán and colleagues derived a formulation including imperfect contact for a shell laminated composite (Guinovart-Sanjuán et al., 2018). Y. Koutsawa et al. developed a micromechanical approach to study imperfect thermal contact (Koutsawa, Karatrantos, Yu, & Ruch, 2018). F. E. Alvarez-Borges et al. describe a gain-enhancement of effective properties for a laminate with imperfect contact (Álvarez-Borges et al., 2018). N. D. Barulich et al. report the effect of damage at the interphase based on a computational micromechanics scheme (Barulich, Godoy, & Dardati, 2016). The nature of interphase is another issue of great interest. The imperfect contact can be studied as an interface with a jump in the normal component of stress, electric displacement and/or magnetic induction, but it can also be described as a “third phase” or an active interphase (Espinosa-Almeyda et al., 2017). In this sense, F. Lebon et al. developed a careful analysis of the interphase soft and hard anisotropic behavior (Lebon et al., 2016).

In the present work, a semi-analytical method is implemented for computing the effective coefficients for periodic three-phase fiber reinforced composite (FRC). Herein, the piezoelectric and piezomagnetic constituents exhibit transversely isotropic properties. In addition, an interphase is considered between the fiber and the matrix in order to study the effect of the quality of the constituent contacts. The periodic cell cross-section is a square with two concentric circles and the periodicity is the same in two perpendicular directions. Section 2 illustrates the mathematical formalism for magneto-electro-elastic (MEE) heterogeneous media for a three-phase FRC. In Section 3, the formulation of homogenized antiplane and plane local problems and effective coefficients obtained by a two-scale asymptotic homogenization method (AHM) is reported. Besides, the semi-analytical approach based on FEM, namely, semi-analytical finite element method (SAFEM) is developed. Herein, the principle of minimum potential energy and the FEM with quadrilateral of eight boundary nodes are combined to find the MEE effective coefficients over 1/4 periodic cell, see Ref. Otero, Rodríguez-Ramos, and Monsivais (2016). In Section 4, numerical analysis and model validation are reported and discussed. Herein, some comparisons between AHM solved via the theory of complex variable and SAFEM allow checking the accuracy of the semi-analytical model. The available data in Refs. Hashemi (2016), Kuo (2011), Yan Jiang, and Song (2013) is also considered for further SAFEM validation.

The main contributions of the present research are the determination of a semi-analytical method (SAFEM) for computing MEE effective moduli of periodic three-phase FRC and the study the effect of interphase thickness and the constituent materials on a composite via SAFEM. In comparison with previous works (Otero et al., 2013, 2016), which only considers an elastic periodic FRC, SAFEM formulation is extended to describe the MEE behavior. New local problems arise and they are solved via minimum potential energy through FEM, in contrast with Refs. Espinosa-Almeyda et al. (2017, 2014) and Guinovart-Díaz et al. (2013) where local problems are solved analytically using AHM via complex variable method. The objective of developing SAFEM is to have a more versatile tool to estimate composite effective properties although the numerical implementation could be somehow heavier than analytical solved AHM.

2. Mathematical formulation for MEE heterogeneous media

A three-phase MEE fiber-reinforced composite (FRC) solid $\Omega\subset\mathbf{R}^3$ with a doubly periodic microstructure is considered (Fig. 1(a)). Here, the reinforcements (fiber and interphase) are unidirectional, infinitely long and concentric cylinders with different radii and material properties. They are periodically distributed without overlapping in the homogeneous matrix. The constituents are made of transversely isotropic materials and belong to the crystal symmetry point group 6mm. The Ox_3- axis of transverse symmetry of each phase coincides with the fiber directions.

The transversal cross-sections of the periodic cell (Y), on the plane Oy_1y_2 with cylindrical axis Oy_3, is characterized by the Cartesian system of coordinates $\{O\,;y_1,y_2,y_3\}$, at the microscale. The local $\mathbf{y}=(y_1,\ y_2,\ y_3)$ and global $\mathbf{x}=(x_1,\ x_2,\ x_3)$ scales are related by $\mathbf{y}=\mathbf{x}/\varepsilon$, where $\varepsilon=l/L$ with $\varepsilon < < 1$ represents the ratio between the periodic cell length (l) and a characteristic macroscopic dimension of the composite (L). The periodic cell structure, i.e. Y, consists of a square with two concentric circles of radius R_2 and $R_1=R_2+t$, where $t>0$ is the thickness of interphase (see, Fig. 1(b)). The regions occupied by the matrix S_1 ($\gamma=1$), interphase S_2 ($\gamma=2$), and fiber S_3 ($\gamma=3$) satisfy $\mathrm{Y}=\bigcup_{\gamma} S_\gamma$ and $\bigcap_{\gamma} S_\gamma=\emptyset$ ($\gamma=1,\ 2,\ 3$). The interface between adjoining phases is defined by $\Gamma_s=\{z:z=R_se^{i\theta},\ 0\le\theta\le2\pi\}$ with $s=1,\ 2$.

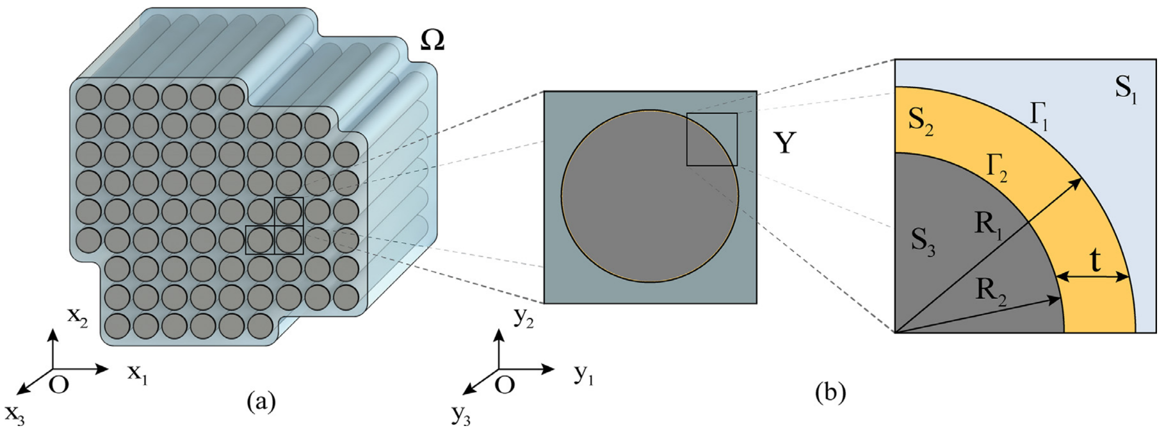

Fig. 1. (a) Representative section of a three-phase fiber-reinforced composite, (b) extracted square transversal cross-sections of the periodic cell.

The static governing equations for a MEE composite Ω, considering the absences of body forces, electric charges, and electric current densities, are defined using partial differential equations system:

$$\begin{aligned}&\left(C_{ijkl}\varepsilon_{kl} - e_{kij}E_k - q_{kij}H_k\right)_{,j} = 0,\\ &(e_{ikl}\,\varepsilon_{kl} + \kappa_{ik}E_k + \alpha_{ik}H_k)_{,i} = 0, \quad \text{in}\,\Omega\\ &(q_{ikl}\,\varepsilon_{kl} + \alpha_{ik}E_k + \mu_{ik}H_k)_{,i} = 0,\end{aligned} \tag{1}$$

Eqs. (1), together with the boundary conditions

$$u_k|_{\partial\Omega} = u_k^0,\ \phi|_{\partial\Omega} = \phi^0,\ \psi|_{\partial\Omega} = \psi^0 \ \text{ on}\,\partial\Omega, \tag{2}$$

where u_k^0, ϕ^0 and ψ^0 are prescribed displacement, electric and magnetic potentials on the boundary of Ω and $i,\ j, k, l = 1,\ 2,\ 3$. Eqs. (1) and (2) represent the fundamental problem associated with the theory of the linear magneto-electro-elasticity heterogeneous structure Ω.

In Eqs. (1) and (2), the coefficients C_{ijkl}, e_{kij}, q_{kij}, κ_{ik}, α_{ik} and μ_{ik} are the elastic stiffness, piezoelectric, piezomagnetic, dielectric permittivity, magnetoelectric coupling and magnetic permeability, respectively. They are functions of local variable **y** in the composite micro-structure. Also, $\varepsilon_{kl} = (u_{k,l} + u_{l,k})/2$, $E_k = -\phi_{,k}$, and $H_k = -\psi_{,k}$ where ε_{kl} and u_i are the strain and mechanical displacement, E_k and ϕ are the electrical field and electrical potential, and H_k and ψ are the magnetical field and magnetical potential, see Ref. Wang, Xia, and Weng (2017). Here, the comma notation indicates partial derivate take the form $(\bullet)_{i,j} = \partial(\bullet)_i/\partial x_j + \varepsilon^{-1}\partial(\bullet)_i/\partial y_j$.

Perfect contact conditions along the interface Γ_s are assumed. They are characterized, as follows:

$$\left[\left[\sigma_{ij}\,n_j\right]\right]_s = 0,\ [[D_i\,n_i]]_s = 0,\ [[B_i\,n_i]]_s = 0,\ \text{on}\,\Gamma_s, \tag{3}$$

$$[[u_k]]_s = 0,\ [[\phi]]_s = 0,\ [[\psi]]_s = 0\ \text{ on}\,\Gamma_s. \tag{4}$$

They describe the fact that the displacement and traction, the quasi-static electric potential and the normal electric displacement, and the quasi-static magnetic potential and normal magnetic induction are continuous across the interfaces between the phases. The notation $[[f]] = 0$ denotes the continuity of f across the interphase Γ_s, i.e., $[[f]]_1 = f^{(1)} - f^{(2)} = 0$ on Γ_1, and $[[f]]_2 = f^{(2)} - f^{(3)} = 0$ on Γ_2. n_i is the component of the outward unit normal vector on Γ_s.

3. Solution of the heterogeneous problems

The homogenized local problems over Y, denoted as ${}_{pq}\mathcal{L}$, ${}_{p}\mathcal{I}$ and ${}_{q}\mathcal{J}$ $(p, q = 1,\ 2,\ 3)$, linked to MEE composites are derived from Eqs. (1)-(4) using the well-known AHM reported in Ref. Pobedrya (1984). For infinitive long fibers, they can be decoupled according to the antiplane and plane deformation state assumed in linear elasticity, that is, ${}_{13}\mathcal{L}$, ${}_{23}\mathcal{L}$, ${}_{1}\mathcal{I}$, ${}_{2}\mathcal{I}$, ${}_{1}\mathcal{J}$ and ${}_{2}\mathcal{J}$ are the antiplane problems and ${}_{11}\mathcal{L}$, ${}_{22}\mathcal{L}$, ${}_{33}\mathcal{L}$, ${}_{12}\mathcal{L}$, ${}_{3}\mathcal{I}$ and ${}_{3}\mathcal{J}$ are plane ones. For the antiplane local problems, this structure exhibits a linear coupling behavior among the anti-plane shear and the in-plane Ox_1x_2 electric and magnetic fields. For the plane ones, the in-plane mechanics displacements are coupled with the anti-plane electric and magnetic fields. Their solutions are required to find the MEE effective moduli of composite.

The asymptotic expansions posing the ansatz:

$$\mathbf{U}(\mathbf{x}) = \mathbf{U}^{(0)}(\mathbf{x},\mathbf{y}) + \varepsilon\,\mathbf{U}^{(1)}(\mathbf{x},\mathbf{y}) + \cdots, \tag{5}$$

Table 1
Local problems with associated local functions and variables.

Local problem	F	${}_F\mathcal{X}_k$	${}_F\mathcal{Y}$	${}_F\mathcal{Z}$	${}_F\mathrm{A}_1$	${}_F\mathrm{A}_2$	${}_F\mathrm{A}_3$
${}_{pq}\mathcal{L}$	pq	${}_{pq}L_k$	${}_{pq}M$	${}_{pq}N$	C_{ijpq}	e_{ipq}	q_{ipq}
${}_p\mathcal{I}$	p	${}_pP_k$	${}_pQ$	${}_pR$	e_{pij}	$-\kappa_{ip}$	$-\alpha_{ip}$
${}_q\mathcal{J}$	q	${}_qS_k$	${}_qT$	${}_qV$	q_{qij}	$-\alpha_{iq}$	$-\mu_{iq}$

where $\mathbf{U} = (u_k,\ \phi,\ \psi)^{\mathrm{T}}$ and the superscripts denote the order of terms in the expansions. Procedure details and rigorous mathematical foundation of AHM can be found in Refs. Camacho-Montes, Rodríguez-Ramos, Bravo-Castillero, Guinovart-Díaz, and Sabina (2006), Camacho-Montes, Sabina, Bravo-Castillero, Guinovart-Díaz, and Rodríguez-Ramos (2009), Sixto-Camacho et al. (2013), and here is omitted.

3.1. Homogenized local problems and effective properties over Y

Twelve homogenized local problems on Y are presented in compact form as:

$$\begin{aligned}
&\left(C_{ijkl}^{(\gamma)}\ {}_F\mathcal{X}_{k,l}^{(\gamma)} + e_{lij}^{(\gamma)}\ {}_F\mathcal{Y}_{,l}^{(\gamma)} + q_{lij}^{(\gamma)}\ {}_F\mathcal{Z}_{,l}^{(\gamma)}\right)_{,j} = -{}_F\mathrm{A}_{1,j}^{(\gamma)}\\
&\left(e_{ikl}^{(\gamma)}\ {}_F\mathcal{X}_{k,l}^{(\gamma)} - \kappa_{il}^{(\gamma)}\ {}_F\mathcal{Y}_{,l}^{(\gamma)} - \alpha_{il}^{(\gamma)}\ {}_F\mathcal{Z}_{,l}^{(\gamma)}\right)_{,i} = -{}_F\mathrm{A}_{2,i}^{(\gamma)}, \quad \text{in}\, S_\gamma\\
&\left(q_{ikl}^{(\gamma)}\ {}_F\mathcal{X}_{k,l}^{(\gamma)} - \alpha_{il}^{(\gamma)}\ {}_F\mathcal{Y}_{,l}^{(\gamma)} - \mu_{il}^{(\gamma)}\ {}_F\mathcal{Z}_{,l}^{(\gamma)}\right)_{,i} = -{}_F\mathrm{A}_{3,i}^{(\gamma)},
\end{aligned} \tag{6}$$

with perfect contact conditions at the interphase

$${}_F\mathcal{X}_k^{(s)} = {}_F\mathcal{X}_k^{(s+1)}, \quad {}_F\mathcal{Y}^{(s)} = {}_F\mathcal{Y}^{(s+1)}, \quad {}_F\mathcal{Z}^{(s)} = {}_F\mathcal{Z}^{(s+1)} \quad \text{on}\, \Gamma_s, \tag{7}$$

$$\begin{aligned}
&\left[{}_F\mathrm{A}_1^{(s)} + C_{ijkl}^{(s)}\ {}_F\mathcal{X}_{k,l}^{(s)} + e_{lij}^{(s)}\ {}_F\mathcal{Y}_{,l}^{(s)} + q_{lij}^{(s)}\ {}_F\mathcal{Z}_{,l}^{(s)}\right] n_j^{(s)}\Big|_{\Gamma_s} =\\
&-\left[{}_F\mathrm{A}_1^{(s+1)} + C_{ijkl}^{(s+1)}\ {}_F\mathcal{X}_{k,l}^{(s+1)} + e_{lij}^{(s+1)}\ {}_F\mathcal{Y}_{,l}^{(s+1)} + q_{lij}^{(s+1)}\ {}_F\mathcal{Z}_{,l}^{(s+1)}\right] n_j^{(s+1)}\Big|_{\Gamma_s},\\
&\left[{}_F\mathrm{A}_2^{(s)} + e_{ikl}^{(s)}\ {}_F\mathcal{X}_{k,l}^{(s)} - \kappa_{il}^{(s)}\ {}_F\mathcal{Y}_{,l}^{(s)} - \alpha_{il}^{(s)}\ {}_F\mathcal{Z}_{,l}^{(s)}\right] n_i^{(s)}\Big|_{\Gamma_s} =\\
&-\left[{}_F\mathrm{A}_2^{(s+1)} + e_{ikl}^{(s+1)}\ {}_F\mathcal{X}_{k,l}^{(s+1)} - \kappa_{il}^{(s+1)}\ {}_F\mathcal{Y}_{,l}^{(s+1)} - \alpha_{il}^{(s+1)}\ {}_F\mathcal{Z}_{,l}^{(s+1)}\right] n_i^{(s+1)}\Big|_{\Gamma_s}, \quad \text{on}\, \Gamma_s\\
&\left[{}_F\mathrm{A}_3^{(s)} + q_{ikl}^{(s)}\ {}_F\mathcal{X}_{k,l}^{(s)} - \alpha_{il}^{(s)}\ {}_F\mathcal{Y}_{,l}^{(s)} - \mu_{il}^{(s)}\ {}_F\mathcal{Z}_{,l}^{(s)}\right] n_i^{(s)}\Big|_{\Gamma_s} =\\
&-\left[{}_F\mathrm{A}_3^{(s+1)} + q_{ikl}^{(s+1)}\ {}_F\mathcal{X}_{k,l}^{(s+1)} - \alpha_{il}^{(s+1)}\ {}_F\mathcal{Y}_{,l}^{(s+1)} - \mu_{il}^{(s+1)}\ {}_F\mathcal{Z}_{,l}^{(s+1)}\right] n_i^{(s+1)}\Big|_{\Gamma_s},
\end{aligned} \tag{8}$$

$$\langle {}_F\mathcal{X}_k \rangle = 0, \quad \langle {}_F\mathcal{Y} \rangle = 0 \quad \text{and} \quad \langle {}_F\mathcal{Z} \rangle = 0, \tag{9}$$

where ${}_F\mathcal{X}_k$ (displacement vector), ${}_F\mathcal{Y}$ (electrical potential) and ${}_F\mathcal{Z}$ (magnetical potential) are the unknown local functions to be found for each local problems over Y. The symbol $\langle f \rangle = |\mathrm{Y}|^{-1} \int_{\mathrm{Y}} f(y)\mathrm{dY}$ represents the volume average per unit length in Y and $(f)_{,\beta} = \partial f / \partial y_\beta$. The pre-index F (pq, p and q) is used to identify local functions (displacements and potentials) associated to the corresponding local problems, which appear below. The local function and variables declared in Eqs. (6)–(9) are summarized in Table 1.

Once the prescribed local problems are solved, the MEE effective coefficients can be determined following the formulae: Associated with the local problems ${}_{pq}\mathcal{L}$,

$$C_{ijpq}^{*} = \left\langle C_{ijpq} + C_{ijkl\,pq}L_{k,l} + e_{lij\,pq}M_{,l} + q_{lij\,pq}N_{,l} \right\rangle, \tag{10}$$

$$e_{ipq}^{*} = \left\langle e_{ipq} + e_{ikl\,pq}L_{k,l} - \kappa_{il\,pq}M_{,l} - \alpha_{il\,pq}N_{,l} \right\rangle, \tag{11}$$

$$q_{ipq}^{*} = \left\langle q_{ipq} + q_{ikl\,pq}L_{k,l} - \alpha_{il\,pq}M_{,l} - \mu_{il\,pq}N_{,l} \right\rangle, \tag{12}$$

Associated with the local problems ${}_p\mathcal{I}$,

$$e_{pij}^{*} = \left\langle e_{pij} + C_{ijkl\,p}P_{k,l} + e_{lij\,p}Q_{,l} + q_{lij\,p}R_{,l} \right\rangle, \tag{13}$$

$$\kappa_{ip}^{*} = \langle \kappa_{ip} - e_{ikl\,p}P_{k,l} + \kappa_{il\,p}Q_{,l} + \alpha_{il\,p}R_{,l} \rangle, \tag{14}$$

$$\alpha_{ip}^{*} = \langle \alpha_{ip} - q_{ikl\,p}P_{k,l} + \alpha_{il\,p}Q_{,l} + \mu_{il\,p}R_{,l} \rangle, \tag{15}$$

Table 2
Local problems and transformation equations.

Local problem	Transformation conditions
${}_{pq}\mathcal{L}$	${}_{pq}L_k = {}_{pq}\hat{L}_k - y_p\delta_{kq},\ {}_{pq}M = {}_{pq}\hat{M},\ {}_{pq}N = {}_{pq}\hat{N}$
${}_{p}\mathcal{I}$	${}_{p}P_k = {}_{p}\hat{P}_k,\ {}_{p}Q = {}_{p}\hat{Q} - y_p,\ {}_{p}R = {}_{p}\hat{R}$
${}_{q}\mathcal{J}$	${}_{q}S_k = {}_{q}\hat{S}_k,\ {}_{q}T = {}_{q}\hat{T},\ {}_{q}V = {}_{q}\hat{V} - y_q$

Table 3
Boundary conditions.

Boundaries	Problem	Boundary conditions	Problem	Boundary conditions
$\{y_1 = d_1,\ y_2\}$ $\{y_1,\ y_2 = d_2\}$	${}_{11}\mathcal{L}$	${}_{11}\hat{L}_1 = y_1,\ {}_{11}\hat{\sigma}_{12} = 0,\ {}_{11}\hat{\sigma}_{21} = 0,\ {}_{11}\hat{L}_2 = 0,$	${}_{22}\mathcal{L}$	${}_{22}\hat{L}_1 = 0,\ {}_{22}\hat{\sigma}_{12} = 0,\ {}_{22}\hat{\sigma}_{21} = 0,\ {}_{22}\hat{L}_2 = y_2,$
$\{y_1 = d_1,\ y_2\}$ $\{y_1,\ y_2 = d_2\}$	${}_{33}\mathcal{L}$	${}_{33}\hat{L}_1 = 0,\ {}_{33}\hat{\sigma}_{12} = 0,\ {}_{33}\hat{\sigma}_{21} = 0,\ {}_{33}\hat{L}_2 = 0$	${}_{13}\mathcal{L}$	${}_{13}\hat{L}_3 = y_1,\ {}_{13}\hat{M} = 0,\ {}_{13}\hat{N} = 0,$ ${}_{13}\hat{\sigma}_{23} = 0,\ {}_{13}\hat{D}_2 = 0,\ {}_{13}\hat{B}_2 = 0,$
$\{y_1 = d_1,\ y_2\}$ $\{y_1,\ y_2 = d_2\}$	${}_{23}\mathcal{L}$	${}_{23}\hat{\sigma}_{13} = 0,\ {}_{23}\hat{D}_1 = 0,\ {}_{23}\hat{B}_1 = 0,$ ${}_{23}\hat{L}_3 = y_2,\ {}_{23}\hat{M} = 0,\ {}_{23}\hat{N} = 0,$	${}_{12}\mathcal{L}$	${}_{12}\hat{L}_2 = y_1,\ {}_{12}\hat{\sigma}_{11} = 0,\ {}_{12}\hat{\sigma}_{22} = 0,\ {}_{12}\hat{\sigma}_{11} = 0,\ {}_{12}\hat{\sigma}_{22} = 0,\ {}_{12}\hat{L}_1 = 0,$
$\{y_1 = d_1,\ y_2\}$ $\{y_1,\ y_2 = d_2\}$	${}_{1}\mathcal{I}$	${}_{1}\hat{P}_3 = 0,\ {}_{1}\hat{Q} = y_1,\ {}_{1}\hat{R} = 0,$ ${}_{1}\hat{\sigma}_{23} = 0,\ {}_{1}\hat{D}_2 = 0,\ {}_{1}\hat{B}_2 = 0,$	${}_{2}\mathcal{I}$	${}_{2}\hat{\sigma}_{13} = 0,\ {}_{2}\hat{D}_1 = 0,\ {}_{2}\hat{B}_1 = 0,$ ${}_{2}\hat{P}_3 = 0,\ {}_{2}\hat{Q} = y_2,\ {}_{2}\hat{R} = 0,$
$\{y_1 = d_1,\ y_2\}$ $\{y_1,\ y_2 = d_2\}$	${}_{3}\mathcal{I}$	${}_{3}\hat{P}_1 = 0,\ {}_{3}\hat{\sigma}_{12} = 0,\ {}_{3}\hat{\sigma}_{21} = 0, {}_{3}\hat{P}_2 = 0,$	${}_{1}\mathcal{J}$	${}_{1}\hat{S}_3 = 0,\ {}_{1}\hat{T} = 0,\ {}_{1}\hat{V} = y_1,$ ${}_{1}\hat{\sigma}_{23} = 0,\ {}_{1}\hat{D}_2 = 0,\ {}_{1}\hat{B}_2 = 0,$
$\{y_1 = d_1,\ y_2\}$ $\{y_1,\ y_2 = d_2\}$	${}_{2}\mathcal{J}$	${}_{2}\hat{\sigma}_{13} = 0,\ {}_{2}\hat{D}_1 = 0,\ {}_{2}\hat{B}_1 = 0,$ ${}_{2}\hat{S}_3 = 0,\ {}_{2}\hat{T} = 0,\ {}_{2}\hat{V} = y_2,$	${}_{3}\mathcal{J}$	${}_{3}\hat{S}_1 = 0,\ {}_{3}\hat{\sigma}_{12} = 0,\ {}_{3}\hat{\sigma}_{21} = 0, {}_{3}\hat{S}_2 = 0,$

Associated with the local problems ${}_{q}\mathcal{J}$,

$$q^*_{qij} = \left\langle q_{qij} + C_{ijkl}\,{}_{q}S_{k,l} + e_{lij}\,{}_{q}T_{,l} + q_{lij\,q}V_{,l}\right\rangle, \tag{16}$$

$$\alpha^*_{iq} = \left\langle \alpha_{iq} - e_{ikl}\,{}_{q}S_{k,l} + \kappa_{il}\,{}_{q}T_{,l} + \alpha_{il\,q}V_{,l}\right\rangle, \tag{17}$$

$$\mu^*_{iq} = \left\langle \mu_{iq} - q_{ikl}\,{}_{q}S_{k,l} + \alpha_{il}\,{}_{q}T_{,l} + \mu_{il\,q}V_{,l}\right\rangle, \tag{18}$$

Notice that the MEE effective coefficients are depending on the local functions (see Table 1) relative to the local problems, Eq. (6)–(9). The local problems Eq. (6)–(9) are solved using two different approaches: the semi-analytical finite element method (SAFEM) and the analytical approach (AHM) via complex variable theory, both methods are described in details in the following sections.

3.2. Semi-analytical approach (SAFEM)

The semi-analytical solution for the local problems is found using FEM, i.e., the local problems (Eqs. (6)–(9)) are solved using FEM via minimum potential energy principle, analogous to the methodology developed by Otero et al. (2013, 2016) for elastic FRC. Thus, MEE effective coefficients can be obtained after transforming local problems into local boundary ones. For that, some spatial symmetry conditions are considered for periodic unit cell and/or constituent material coefficients. This way, the numerical procedure is simplified.

Therefore, the semi-analytical solution of local problems can be simplified, i.e., Eqs. (6)–(9) are transformed into boundary value problems over 1/4 of periodic cell Y. Besides, the material properties are taken as even functions with respect to the local coordinate system y_i, and conditions are satisfied for the local functions summarized in Table 2, see Ref. Bakhvalov and Panasenko (1989).

From now on, the caret symbol superscript over the local functions, ${}_{F}\hat{\sigma}_{ij}$, ${}_{F}\hat{D}_i$ and ${}_{F}\hat{B}_i$ denotes its equivalent representations on 1/4 of Y.

Then, substituting the relations of Table 2 into Eq. (6), the corresponding boundary value problems are reduced to:

$${}_{F}\hat{\sigma}^{(\gamma)}_{ij,j} = 0,\quad {}_{F}\hat{D}^{(\gamma)}_{i,i} = 0,\quad {}_{F}\hat{B}^{(\gamma)}_{i,i} = 0, \tag{19}$$

where ${}_{F}\hat{\sigma}^{(\gamma)}_{ij} = C^{(\gamma)}_{ijkl}\,{}_{F}\hat{\mathcal{X}}^{(\gamma)}_{k,l} + e^{(\gamma)}_{lij}\,{}_{F}\hat{\mathcal{Y}}^{(\gamma)}_{,l} + q^{(\gamma)}_{lij}\,{}_{F}\hat{\mathcal{Z}}^{(\gamma)}_{,l}$, ${}_{F}\hat{D}^{(\gamma)}_{i} = e^{(\gamma)}_{ikl}\,{}_{F}\hat{\mathcal{X}}^{(\gamma)}_{k,l} - \kappa^{(\gamma)}_{il}\,{}_{F}\hat{\mathcal{Y}}^{(\gamma)}_{,l} - \alpha^{(\gamma)}_{il}\,{}_{F}\hat{\mathcal{Z}}^{(\gamma)}_{,l}$ and ${}_{F}\hat{B}^{(\gamma)}_{i} = q^{(\gamma)}_{ikl}\,{}_{F}\hat{\mathcal{X}}^{(\gamma)}_{k,l} - \alpha^{(\gamma)}_{il}\,{}_{F}\hat{\mathcal{Y}}^{(\gamma)}_{,l} - \mu^{(\gamma)}_{il}\,{}_{F}\hat{\mathcal{Z}}^{(\gamma)}_{,l}$. Here, ${}_{F}\hat{\mathcal{X}}_k$, ${}_{F}\hat{\mathcal{Y}}$ and ${}_{F}\hat{\mathcal{Z}}$ are the new local pseudo-displacements and pseudo-potentials over 1/4 of periodic cell Y, respectively. The boundary conditions associated with the boundary value problems are summarized in Table 3. In addition, $d_h = \{0,\ l_h\}$ where l_h with $h = 1,\ 2$ is the periodic cell length in the direction y_h. Also, the prescribed boundaries of 1/4 of Y are $\{y_1 = d_1,\ y_2\} \equiv \left\{(y_1,\ y_2) \in \mathbb{R}^2 | y_1 = \{0,\ l_1\},\ \ 0 \le y_2 \le l_2\right\}$ and $\{y_1,\ y_2 = d_2\} \equiv \left\{(y_1,\ y_2) \in \mathbb{R}^2 \middle| 0 \le y_1 \le l_1,\ \ y_2 = \{0, l_2\}\right\}$.

Likewise, the corresponding MEE effective coefficients, Eqs. (10)–(18), over Y are rewritten as:

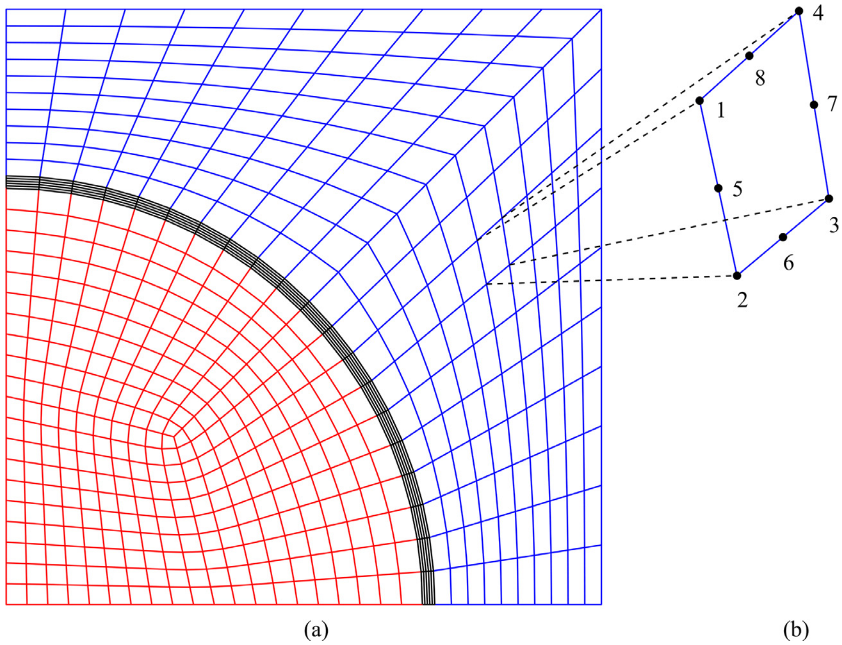

Fig. 2. a) Representative geometric mesh for a quarter of Y, and b) quadrilateral area element of 8 nodes.

Associated with the local problem ${}_{pq}\mathcal{L}$,

$$\begin{aligned} C^*_{ijpq} &= 4\left\langle C_{ijkl}\,{}_{pq}\hat{L}_{k,l} + e_{lij}\,{}_{pq}\hat{M}_{,l} + q_{lij}\,{}_{pq}\hat{N}_{,l}\right\rangle, \\ e^*_{ipq} &= 4\left\langle e_{ikl}\,{}_{pq}\hat{L}_{k,l} - \kappa_{il}\,{}_{pq}\hat{M}_{,l} - \alpha_{il}\,{}_{pq}\hat{N}_{,l}\right\rangle, \\ q^*_{ipq} &= 4\left\langle q_{ikl}\,{}_{pq}\hat{L}_{k,l} - \alpha_{il}\,{}_{pq}\hat{M}_{,l} - \mu_{il}\,{}_{pq}\hat{N}_{,l}\right\rangle. \end{aligned} \tag{20}$$

Associated with the local problem ${}_{p}\mathcal{I}$,

$$\begin{aligned} e^*_{pij} &= 4\langle C_{ijkl}\,{}_{p}\hat{P}_{k,l} + e_{lij}\,{}_{p}\hat{Q}_{,l} + q_{lij}\,{}_{p}\hat{R}_{,l}\rangle, \\ \kappa^*_{ip} &= 4\langle -e_{ikl}\,{}_{p}\hat{P}_{k,l} + \kappa_{il}\,{}_{p}\hat{Q}_{,l} + \alpha_{il}\,{}_{p}\hat{R}_{,l}\rangle, \\ \alpha^*_{ip} &= 4\langle -q_{ikl}\,{}_{p}\hat{P}_{k,l} + \alpha_{il}\,{}_{p}\hat{Q}_{,l} + \mu_{il}\,{}_{p}\hat{R}_{,l}\rangle. \end{aligned} \tag{21}$$

Associated with the local problem ${}_{q}\mathcal{J}$,

$$\begin{aligned} q^*_{qij} &= 4\left\langle C_{ijkl}\,{}_{q}\hat{S}_{k,l} + e_{lij}\,{}_{q}\hat{T}_{,l} + q_{lij}\,{}_{q}\hat{V}_{,l}\right\rangle, \\ \alpha^*_{iq} &= 4\left\langle -e_{ikl}\,{}_{q}\hat{S}_{k,l} + \kappa_{il}\,{}_{q}\hat{T}_{,l} + \alpha_{il}\,{}_{q}\hat{V}_{,l}\right\rangle, \\ \mu^*_{iq} &= 4\left\langle -q_{ikl}\,{}_{q}\hat{S}_{k,l} + \alpha_{il}\,{}_{q}\hat{T}_{,l} + \mu_{il}\,{}_{q}\hat{V}_{,l}\right\rangle. \end{aligned} \tag{22}$$

3.2.1. Finite element method implementation for local problems

The quarter of Y is meshed with a finite number of quadrilateral area elements of eight nodes (see Fig. 2). Each quadrilateral area element is characterized by four nodes located at the vertices and the remaining ones at the midpoints of the edges. Also, each node is associated with a pseudo-displacements-potential vector $({}_F\hat{\mathcal{X}}_k,\ {}_F\hat{\mathcal{Y}},\ {}_F\hat{\mathcal{Z}})^{\mathrm{T}}$ linked with the local problem to be solved, where the pseudo-displacements ${}_F\hat{\mathcal{X}}_k$, and the electric and magnetic pseudo-potentials (i.e., ${}_F\hat{\mathcal{Y}}$ and ${}_F\hat{\mathcal{Z}}$) are written taking the shape functions as local base whose coefficients are the nodal values of the unknown displacement fields. Then, we have:

$${}_F\hat{\mathcal{X}}_1 = \psi_s q_{1s},\quad {}_F\hat{\mathcal{X}}_2 = \psi_s q_{2s},\quad {}_F\hat{\mathcal{X}}_3 = \psi_s q_{3s},\quad {}_F\hat{\mathcal{Y}} = \psi_s q_{4s},\quad {}_F\hat{\mathcal{Z}} = \psi_s q_{5s}, \tag{23}$$

where, q_{ms} is the *m-th* component of $({}_F\hat{\mathcal{X}}_k,\ {}_F\hat{\mathcal{Y}},\ {}_F\hat{\mathcal{Z}})^{\mathrm{T}}$ on the *s-th* node of element with $m = 1, \cdots, 5$ and $s = 1, \cdots, 8$.

In addition, ψ_s are element's shape functions defined as

$$\begin{aligned} &\psi_1 = \tau_1\eta_1 c_1, \quad \psi_2 = \tau_3\eta_1, \quad \psi_3 = \tau_2\eta_1 c_2, \quad \psi_4 = \tau_2\eta_3, \\ &\psi_5 = \tau_2\eta_2 c_3, \quad \psi_6 = \tau_3\eta_2, \quad \psi_7 = \tau_1\eta_2 c_4, \quad \psi_8 = \tau_1\eta_3, \end{aligned} \tag{24}$$

with $\tau_1 = (1-\zeta_1)/2$, $\tau_2 = (1+\zeta_1)/2$, $\tau_3 = 1-{\zeta_1}^2$, $\eta_1 = (1-\zeta_2)/2$, $\eta_2 = (1+\zeta_2)/2$, $\eta_3 = 1-{\zeta_2}^2$, $c_1 = -1-\zeta_1-\zeta_2$, $c_2 = -1+\zeta_1-\zeta_2$, $c_3 = -1+\zeta_1+\zeta_2$ and $c_4 = -1-\zeta_1+\zeta_2$. Herein, ζ_1 and ζ_2 are the element's natural coordinates, see Ref. Zienkiewicz, Taylor, and Zhu (2013).

3.2.2. Antiplane local problem solutions

The antiplane local problem ${}_{13}\mathcal{L}$, ${}_{23}\mathcal{L}$, ${}_{1}\mathcal{I}$, ${}_{2}\mathcal{I}$, ${}_{1}\mathcal{J}$ and ${}_{2}\mathcal{J}$ are solved as follow. From now on, the dependence of pre-index F is omitted to simplify the notation.

In the boundary value problems, Eq. (19), the antiplane shear stress and the in-plane electric displacement and magnetic induction satisfy the relations written in matrix form

$$\hat{\boldsymbol{\sigma}} = \mathbf{C}\,\hat{\boldsymbol{\varepsilon}} - \mathbf{e}\,\widehat{\mathbf{E}} - \mathbf{q}\,\widehat{\mathbf{H}},\ \widehat{\mathbf{D}} = \mathbf{e}^{\mathrm{T}}\,\hat{\boldsymbol{\varepsilon}} + \boldsymbol{\kappa}\,\widehat{\mathbf{E}} + \boldsymbol{\alpha}\,\widehat{\mathbf{H}},\ \widehat{\mathbf{B}} = \mathbf{q}^{\mathrm{T}}\,\hat{\boldsymbol{\varepsilon}} + \boldsymbol{\alpha}\,\widehat{\mathbf{E}} + \boldsymbol{\mu}\,\widehat{\mathbf{H}} \tag{25}$$

where, $\hat{\boldsymbol{\sigma}} = \left(\hat{\sigma}_{13}\ \hat{\sigma}_{23}\right)^{\mathrm{T}}$, $\hat{\mathbf{D}} = \left(\hat{D}_1\ \hat{D}_2\right)^{\mathrm{T}}$, $\hat{\mathbf{B}} = (\hat{B}_1\ \hat{B}_2)^{\mathrm{T}}$, $\hat{\boldsymbol{\varepsilon}} = \left(\hat{\mathcal{X}}_{3,1}\quad \hat{\mathcal{X}}_{3,2}\right)^{\mathrm{T}}$, $\hat{\mathbf{E}} = -(\hat{\mathcal{Y}}_{,1}\quad \hat{\mathcal{Y}}_{,2})^{\mathrm{T}}$, $\hat{\mathbf{H}} = -(\hat{\mathcal{Z}}_{,1}\quad \hat{\mathcal{Z}}_{,2})^{\mathrm{T}}$, $\mathbf{C} = \begin{pmatrix} C_{1313} & 0 \\ 0 & C_{2323}\end{pmatrix}$, $\mathbf{e} = \begin{pmatrix} e_{113} & 0 \\ 0 & e_{223}\end{pmatrix}$, $\mathbf{q} = \begin{pmatrix} q_{113} & 0 \\ 0 & q_{223}\end{pmatrix}$, $\boldsymbol{\kappa} = \begin{pmatrix} \kappa_{11} & 0 \\ 0 & \kappa_{22}\end{pmatrix}$, $\boldsymbol{\alpha} = \begin{pmatrix} \alpha_{11} & 0 \\ 0 & \alpha_{22}\end{pmatrix}$ and $\boldsymbol{\mu} = \begin{pmatrix} \mu_{11} & 0 \\ 0 & \mu_{22}\end{pmatrix}$.

The constitutive relations for the antiplane problems are unified in Eq. (25), the only difference is focused on the local functions $\hat{\mathcal{X}}_3$, $\hat{\mathcal{Y}}$ and $\hat{\mathcal{Z}}$ associated to each local problems, see Table 1.

Then, the solution of each previously described antiplane boundary value problems consist in finding the associated $\hat{\mathcal{X}}_3$, $\hat{\mathcal{Y}}$ and $\hat{\mathcal{Z}}$ in the form of Eq. (23), which minimizes the potential energy U. The total corresponding potential energy U for a MEE solid body Ω is defined as:

$$\mathrm{U} = \frac{1}{2}\int_{\Omega} \sigma_{ij}\varepsilon_{ij} dV - \frac{1}{2}\int_{\Omega} D_i E_i\, dV - \frac{1}{2}\int_{\Omega} B_i H_i\, dV\ (i, j = 1, 2, 3). \tag{26}$$

This Eq. (26) involves the strain energy per unit volume in the body, and the energies associated with the contributions of the effects of the electric and magnetic fields. Besides, the absences of body forces, electric charges, and electric current densities are assumed. Therefore, the total energy related to the element e denoted as region Ω_e, is found by:

$$\mathrm{U}_e = \frac{1}{2}\int_{\Omega_e} \hat{\boldsymbol{\sigma}}^{\mathrm{T}}\,\hat{\boldsymbol{\varepsilon}}\, dV_e - \frac{1}{2}\int_{\Omega_e} \widehat{\mathbf{D}}^{\mathrm{T}}\,\widehat{\mathbf{E}}\, dV_e - \frac{1}{2}\int_{\Omega_e} \widehat{\mathbf{B}}^{\mathrm{T}}\,\widehat{\mathbf{H}}\, dV_e. \tag{27}$$

Consequently, the strain–displacement, the electric field–electric potential, and the magnetic field–magnetic potential relations are usually written as functions of the natural coordinates and the element's shape functions:

$$\hat{\boldsymbol{\varepsilon}} = \mathbf{B}_{\boldsymbol{\varepsilon}}\,\mathbf{Q},\ \widehat{\mathbf{E}} = -\,\mathbf{B}_{\mathbf{E}}\,\mathbf{Q},\ \widehat{\mathbf{H}} = -\,\mathbf{B}_{\mathbf{H}}\,\mathbf{Q}. \tag{28}$$

where $\mathbf{Q} = [q_{31}\quad q_{41}\quad q_{51}\quad \cdots\quad q_{38}\quad q_{48}\quad q_{58}]^{\mathrm{T}}$ is the element node vector. The matrices $\mathbf{B}_{\varepsilon}$, $\mathbf{B}_{\mathbf{E}}$ and $\mathbf{B}_{\mathbf{H}}$, of order 2×24, are defined as a function of $J_{11}, J_{12}, J_{21}, J_{22}$ and the derivate of the element's shape functions, as follows

$$\mathbf{B}_{\boldsymbol{\varepsilon}} = \begin{pmatrix} J_{11} & J_{12} \\ J_{21} & J_{22}\end{pmatrix}\begin{pmatrix} \frac{\partial\psi_1}{\partial\zeta_1} & 0 & 0 & \frac{\partial\psi_2}{\partial\zeta_1} & 0 & 0 & \cdots & \frac{\partial\psi_7}{\partial\zeta_1} & 0 & 0 & \frac{\partial\psi_8}{\partial\zeta_1} & 0 & 0 \\ \frac{\partial\psi_1}{\partial\zeta_2} & 0 & 0 & \frac{\partial\psi_2}{\partial\zeta_2} & 0 & 0 & \cdots & \frac{\partial\psi_7}{\partial\zeta_2} & 0 & 0 & \frac{\partial\psi_8}{\partial\zeta_2} & 0 & 0 \end{pmatrix},$$

$$\mathbf{B}_{\mathbf{E}} = \begin{pmatrix} J_{11} & J_{12} \\ J_{21} & J_{22}\end{pmatrix}\begin{pmatrix} 0 & \frac{\partial\psi_1}{\partial\zeta_1} & 0 & 0 & \frac{\partial\psi_2}{\partial\zeta_1} & 0 & \cdots & 0 & \frac{\partial\psi_7}{\partial\zeta_1} & 0 & 0 & \frac{\partial\psi_8}{\partial\zeta_1} & 0 \\ 0 & \frac{\partial\psi_1}{\partial\zeta_2} & 0 & 0 & \frac{\partial\psi_2}{\partial\zeta_2} & 0 & \cdots & 0 & \frac{\partial\psi_7}{\partial\zeta_2} & 0 & 0 & \frac{\partial\psi_8}{\partial\zeta_2} & 0 \end{pmatrix} \text{ and}$$

$$\mathbf{B}_{\mathbf{H}} = \begin{pmatrix} J_{11} & J_{12} \\ J_{21} & J_{22}\end{pmatrix}\begin{pmatrix} 0 & 0 & \frac{\partial\psi_1}{\partial\zeta_1} & 0 & 0 & \frac{\partial\psi_2}{\partial\zeta_1} & \cdots & 0 & 0 & \frac{\partial\psi_7}{\partial\zeta_1} & 0 & 0 & \frac{\partial\psi_8}{\partial\zeta_1} \\ 0 & 0 & \frac{\partial\psi_1}{\partial\zeta_2} & 0 & 0 & \frac{\partial\psi_2}{\partial\zeta_2} & \cdots & 0 & 0 & \frac{\partial\psi_7}{\partial\zeta_2} & 0 & 0 & \frac{\partial\psi_8}{\partial\zeta_2} \end{pmatrix},$$

where $J_{11}, J_{12}, J_{21}, J_{22}$ are the inverse matrix coefficients of Jacobian transformation $\mathbf{J}$ between the Cartesian system $\{y_1, y_2\}$ and the natural coordinates system $\{\zeta_1, \zeta_2\}$.

Analogously, stress, electric displacement and magnetic induction values are determined, as follow

$$\hat{\boldsymbol{\sigma}} = [\mathbf{C}\,\mathbf{B}_{\boldsymbol{\varepsilon}}\ + \mathbf{e}\,\mathbf{B}_{\mathbf{E}}\ + \mathbf{q}\,\mathbf{B}_{\mathbf{H}}]\mathbf{Q},\ \hat{\mathbf{D}} = \left[\mathbf{e}^{\mathbf{T}}\,\mathbf{B}_{\boldsymbol{\varepsilon}}\ - \boldsymbol{\kappa}\,\mathbf{B}_{\mathbf{E}}\ - \boldsymbol{\alpha}\,\mathbf{B}_{\mathbf{H}}\right]\mathbf{Q},\ \hat{\mathbf{B}} = \left[\mathbf{q}^{\mathbf{T}}\,\mathbf{B}_{\boldsymbol{\varepsilon}}\ - \boldsymbol{\alpha}\,\mathbf{B}_{\mathbf{E}}\ - \boldsymbol{\mu}\mathbf{B}_{\mathbf{H}}\right]\mathbf{Q}. \tag{29}$$

Then, substituting Eqs. (28) and (29) into Eq. (27), we obtain the total energy in the form:

$$\mathrm{U}_e = \frac{1}{2}\,\mathbf{Q}^{\mathrm{T}}\mathbf{K}_e\mathbf{Q}, \tag{30}$$

where

$$\mathbf{K}_e = t_e\int_{-1}^{1}\int_{-1}^{1} [\mathbf{B}_{\mathbf{C}}\,\mathbf{B}_{\boldsymbol{\varepsilon}}\ + \mathbf{B}_{\kappa}\,\mathbf{B}_{\mathbf{E}}\ + \mathbf{B}_{\mu}\mathbf{B}_{\mathbf{H}}]\, det\,(\mathbf{J})\, d\zeta_1 d\zeta_2, \tag{31}$$

is the element matrix of MEE properties. In addition, $\mathbf{B}_{\mathbf{C}} = {\mathbf{B}_{\boldsymbol{\varepsilon}}}^{\mathrm{T}}\mathbf{C}^{\mathrm{T}} + {\mathbf{B}_{\mathbf{E}}}^{\mathrm{T}}\mathbf{e}^{\mathrm{T}} + {\mathbf{B}_{\mathbf{H}}}^{\mathrm{T}}\mathbf{q}^{\mathrm{T}}$, $\mathbf{B}_{\kappa} = \mathbf{B}_{\boldsymbol{\varepsilon}}^{\mathrm{T}}\mathbf{e} - {\mathbf{B}_{\mathbf{E}}}^{\mathrm{T}}\boldsymbol{\kappa}^{\mathrm{T}} - {\mathbf{B}_{\mathbf{H}}}^{\mathrm{T}}\boldsymbol{\alpha}^{\mathrm{T}}$, $\mathbf{B}_{\mu} = {\mathbf{B}_{\boldsymbol{\varepsilon}}}^{\mathrm{T}}\mathbf{q} - {\mathbf{B}_{\mathbf{E}}}^{\mathrm{T}}\boldsymbol{\alpha}^{\mathrm{T}} - {\mathbf{B}_{\mathbf{H}}}^{\mathrm{T}}\boldsymbol{\mu}^{\mathrm{T}}$, and t_e is the thickness constant over the element.

Therefore, if we use the connectivity of the elements, then the MEE total energy Π in the body results equals to:

$$\Pi = \sum_{e}\frac{1}{2}\,\mathbf{Q}^{\mathrm{T}}\mathbf{K}_e\mathbf{Q} = \frac{1}{2}\,\hat{\mathbf{Q}}^{\mathrm{T}}\mathbf{K}\hat{\mathbf{Q}}. \tag{32}$$

In Eq. (32), $\mathbf{K}$ and $\hat{\mathbf{Q}}$ represents the MEE properties global matrix and the pseudo-displacement-potentials global vector on Y. The minimization of Π (Eq. (32)) is determined by solving an algebraic system of equations obtained by deriving Π with respect to the global vector, setting the equations equal to cero and applying the corresponding boundary conditions of each local problem. Then, through Eqs. (33)–(35), the solution is used to find the associated effective coefficients.

The antiplane MEE effective properties can be found substituting the derivate $\hat{\mathcal{X}}_{3,\beta}$, $\hat{\mathcal{Y}}_{,\beta}$ and $\hat{\mathcal{Z}}_{,\beta}$ $(\beta = 1,\ 2)$, as functions of the natural coordinates and the element's shape functions into the Eqs. (20)–(22), thus

$$\begin{cases} C^*_{\alpha 3\alpha 3} = 4\displaystyle\int_0^1\int_0^{1-\zeta_1} \mathbf{D}_a\,\mathbf{B}_a\,\mathbf{Q}\,\det(\mathbf{J})d\zeta_1 d\zeta_2, \\ e^*_{\alpha\alpha 3} = 4\displaystyle\int_0^1\int_0^{1-\zeta_1} \mathbf{C}_a\,\mathbf{B}_a\,\mathbf{Q}\,\det(\mathbf{J})d\zeta_1 d\zeta_2, \quad \text{for the local problems}\,{}_{\alpha 3}\mathcal{L}, \\ q^*_{\alpha\alpha 3} = 4\displaystyle\int_0^1\int_0^{1-\zeta_1} \mathbf{G}_a\,\mathbf{B}_a\,\mathbf{Q}\,\det(\mathbf{J})d\zeta_1 d\zeta_2, \end{cases} \tag{33}$$

$$\begin{cases} e^*_{\alpha\alpha 3} = 4\displaystyle\int_0^1\int_0^{1-\zeta_1} \mathbf{D}_a\,\mathbf{B}_a\,\mathbf{Q}\,\det(\mathbf{J})d\zeta_1 d\zeta_2, \\ \kappa^*_{\alpha\alpha} = 4\displaystyle\int_0^1\int_0^{1-\zeta_1} \mathbf{C}_a\,\mathbf{B}_a\,\mathbf{Q}\,\det(\mathbf{J})d\zeta_1 d\zeta_2, \quad \text{for the local problems}\,{}_{\alpha}\mathcal{I}, \\ \alpha^*_{\alpha\alpha} = 4\displaystyle\int_0^1\int_0^{1-\zeta_1} \mathbf{G}_a\,\mathbf{B}_a\,\mathbf{Q}\,\det(\mathbf{J})d\zeta_1 d\zeta_2, \end{cases} \tag{34}$$

$$\begin{cases} q^*_{\alpha\alpha 3} = 4\displaystyle\int_0^1\int_0^{1-\zeta_1} \mathbf{D}_a\,\mathbf{B}_a\,\mathbf{Q}\,\det(\mathbf{J})d\zeta_1 d\zeta_2, \\ \alpha^*_{\alpha\alpha} = 4\displaystyle\int_0^1\int_0^{1-\zeta_1} \mathbf{C}_a\,\mathbf{B}_a\,\mathbf{Q}\,\det(\mathbf{J})d\zeta_1 d\zeta_2, \quad \text{for the local problems}\,{}_{\alpha}\mathcal{J}, \\ \mu^*_{\alpha\alpha} = 4\displaystyle\int_0^1\int_0^{1-\zeta_1} \mathbf{G}_a\,\mathbf{B}_a\,\mathbf{Q}\,\det(\mathbf{J})d\zeta_1 d\zeta_2, \end{cases} \tag{35}$$

where the vectors $\mathbf{D}_a$, $\mathbf{C}_a$, $\mathbf{G}_a$ and the matrix $\mathbf{B}_a$ are referred to antiplane problem defined in Appendix A.

3.2.3. Plane local problem solutions

Here, the plane local problems ${}_{11}\mathcal{L}$, ${}_{22}\mathcal{L}$, ${}_{33}\mathcal{L}$, ${}_{12}\mathcal{L}$, ${}_{3}\mathcal{I}$ and ${}_{3}\mathcal{J}$ are determined. The solutions of those problems are similar. Therefore, only the plane local problem ${}_{\beta\beta}\mathcal{L}$ (the problems ${}_{pq}\mathcal{L}$ when $p = q$, i.e., $\beta\beta = 11, 22, 33$) is solved, in a similar way to above reported antiplane problem.

The Eq. (19) can be written in matrix form as

$${}_{\beta\beta}\hat{\boldsymbol{\sigma}} = {}_{\beta\beta}\mathbf{C}_p\,{}_{\beta\beta}\hat{\boldsymbol{\varepsilon}} \tag{36}$$

where, ${}_{\beta\beta}\hat{\boldsymbol{\sigma}} = ({}_{\beta\beta}\hat{\sigma}_{11} \quad {}_{\beta\beta}\hat{\sigma}_{22} \quad {}_{\beta\beta}\hat{\sigma}_{12})^{\mathrm{T}}$, ${}_{\beta\beta}\hat{\boldsymbol{\varepsilon}} = ({}_{\beta\beta}\hat{L}_{1,1} \quad {}_{\beta\beta}\hat{L}_{2,2} \quad {}_{\beta\beta}\hat{L}_{1,2}+{}_{\beta\beta}\hat{L}_{2,1})^{\mathrm{T}}$ and ${}_{\beta\beta}\mathbf{C}_p = \begin{pmatrix} C_{1111} & C_{1122} & 0 \\ C_{2211} & C_{2222} & 0 \\ 0 & 0 & C_{1212} \end{pmatrix}$. Henceforth, the pre-index $\beta\beta$ is omitted to simplify the notation. As can be seen, the plane local problem statements are exactly the same as in elastic composite case, see Otero et al. (2013, 2016).

To find the solution of the problems ${}_{\beta\beta}\mathcal{L}$, the unknown pseudo-displacements $\hat{L}_1$ and $\hat{L}_2$ which minimizes the corresponding potential energy, Eq. (26), needs to be calculated.

Then, using the relations Eqs. (23), we have

$$\mathrm{U}_e = \frac{1}{2}\int_{\Omega_e} \boldsymbol{\sigma}^{\mathrm{T}}\boldsymbol{\varepsilon}\, dV_e, \ \boldsymbol{\sigma} = \mathbf{C}_p\,\mathbf{B}_p\,\mathbf{Q}_1 \text{ and } \boldsymbol{\varepsilon} = \mathbf{B}_p\,\mathbf{Q}_1. \tag{37}$$

In Eq. (37), $\mathbf{Q}_1 = [\ q_{11} \quad q_{21} \quad q_{12} \quad q_{22} \quad \cdots \quad q_{17} \quad q_{27} \quad q_{18} \quad q_{28}\ ]^{\mathrm{T}}$ represents the nodal values displacement vector and the matrix $\mathbf{B}_p$ is referred to plane problems, such that

$$\mathbf{B}_p = \begin{pmatrix} J_{11} & J_{12} & 0 & 0 \\ 0 & 0 & J_{21} & J_{22} \\ J_{21} & J_{22} & J_{11} & J_{12} \end{pmatrix} \times \begin{pmatrix} \frac{\partial\psi_1}{\partial\zeta_1} & 0 & \frac{\partial\psi_2}{\partial\zeta_1} & 0 & \frac{\partial\psi_3}{\partial\zeta_1} & 0 & \frac{\partial\psi_4}{\partial\zeta_1} & 0 & \frac{\partial\psi_5}{\partial\zeta_1} & 0 & \frac{\partial\psi_6}{\partial\zeta_1} & 0 & \frac{\partial\psi_7}{\partial\zeta_1} & 0 & \frac{\partial\psi_8}{\partial\zeta_1} & 0 \\ \frac{\partial\psi_1}{\partial\zeta_2} & 0 & \frac{\partial\psi_2}{\partial\zeta_2} & 0 & \frac{\partial\psi_3}{\partial\zeta_2} & 0 & \frac{\partial\psi_4}{\partial\zeta_2} & 0 & \frac{\partial\psi_5}{\partial\zeta_2} & 0 & \frac{\partial\psi_6}{\partial\zeta_2} & 0 & \frac{\partial\psi_7}{\partial\zeta_2} & 0 & \frac{\partial\psi_8}{\partial\zeta_2} & 0 \\ 0 & \frac{\partial\psi_1}{\partial\zeta_1} & 0 & \frac{\partial\psi_2}{\partial\zeta_1} & 0 & \frac{\partial\psi_3}{\partial\zeta_1} & 0 & \frac{\partial\psi_4}{\partial\zeta_1} & 0 & \frac{\partial\psi_5}{\partial\zeta_1} & 0 & \frac{\partial\psi_6}{\partial\zeta_1} & 0 & \frac{\partial\psi_7}{\partial\zeta_1} & 0 & \frac{\partial\psi_8}{\partial\zeta_1} \\ 0 & \frac{\partial\psi_1}{\partial\zeta_2} & 0 & \frac{\partial\psi_2}{\partial\zeta_2} & 0 & \frac{\partial\psi_3}{\partial\zeta_2} & 0 & \frac{\partial\psi_4}{\partial\zeta_2} & 0 & \frac{\partial\psi_5}{\partial\zeta_2} & 0 & \frac{\partial\psi_6}{\partial\zeta_2} & 0 & \frac{\partial\psi_7}{\partial\zeta_2} & 0 & \frac{\partial\psi_8}{\partial\zeta_2} \end{pmatrix}. \tag{38}$$

Therefore, the energy associated to one plane element is $U_e = \frac{1}{2}\mathbf{Q}_1^T\mathbf{K}_e\mathbf{Q}_1$, as a results of combining the expressions of Eq. (37). Here, $\mathbf{K}_e = t_e\int_{-1}^{1}\int_{-1}^{1}\mathbf{B}_p^T\mathbf{C}_p^T\mathbf{B}_p\, det\,(\mathrm{J})\, d\zeta_1 d\zeta_2$ is the element stiffness matrix.

Consequently, the total strain potential energy analogous to Eq. (32), taking into account the contribution of all elements, is defined as

$$\Pi = \sum_e \frac{1}{2}\,\mathbf{Q}_1^T\,\mathbf{K}_e\,\mathbf{Q}_1 \; = \frac{1}{2}\,\hat{\mathbf{Q}}_1^T\mathbf{K}\hat{\mathbf{Q}}_1, \tag{39}$$

where $\mathbf{K}$ is the MEE properties global matrix and $\hat{\mathbf{Q}}_1$ is the global displacement vector.

The solution of Eq. (39) is obtained similarly to the system solution Eq. (32) using the corresponding boundary conditions referred to problem $_{\beta\beta}\mathcal{L}$, see Table 3.

The MEE effective properties associated to this problem can be found replacing the derivatives $\hat{L}_{1,1}$, $\hat{L}_{2,2}$, $\hat{L}_{1,2}$ and $\hat{L}_{2,1}$ as functions of the natural coordinates and the element's shape functions, Eq. (24), into Eq. (20). Thus, the effective properties are defined as follows:

$$\mathbf{C}^* = 4\langle \mathbf{D}_p\,\mathbf{B}_p\,\mathbf{Q}_1\rangle = 4\int_0^1\int_0^{1-\zeta_1}\mathbf{D}_p\,\mathbf{B}_p\,\mathbf{Q}_1 \det(\mathbf{J})\, d\zeta_1 d\zeta_2. \tag{40}$$

where

$$\mathbf{C}^* = \begin{pmatrix} C^*_{1111} & C^*_{2211} & C^*_{3311} & C^*_{1211} & e^*_{311} & q^*_{311}\end{pmatrix}^T, \text{ associated to the local problems }{}_{11}\mathcal{L}, \tag{41}$$

$$\mathbf{C}^* = \begin{pmatrix} C^*_{1122} & C^*_{2222} & C^*_{3322} & C^*_{1222} & e^*_{322} & q^*_{322}\end{pmatrix}^T, \text{ associated to the local problems }{}_{22}\mathcal{L}, \tag{42}$$

$$\mathbf{C}^* = \begin{pmatrix} C^*_{1133} & C^*_{2233} & C^*_{3333} & C^*_{1233} & e^*_{333} & q^*_{333}\end{pmatrix}^T, \text{ associated to the local problems }{}_{33}\mathcal{L}, \tag{43}$$

the matrix $\mathbf{B}_p$ is define in Eq. (38), $\mathbf{D}_p = \begin{pmatrix} C_{1111} & C_{2211} & C_{3311} & 0 & e_{311} & q_{311} \\ C_{1122} & C_{2222} & C_{3322} & 0 & e_{322} & q_{322} \\ 0 & 0 & 0 & C_{1212} & 0 & 0 \end{pmatrix}^T$ and $\mathbf{Q}_1$ is the nodal values displacement vector associated to the plane local problem $_{\beta\beta}\mathcal{L}$.

The solution of the local problems $_{12}\mathcal{L}$, $_3\mathcal{I}$ and $_3\mathcal{J}$ follows straightforward from the above procedure, interchanging the pre-index $\beta\beta$ by 12 or 3, and considering the pseudo-displacement local functions of each problem $_{12}\hat{L}_1$ and $_{12}\hat{L}_2$, $_3\hat{P}_1$ and $_3\hat{P}_2$, $_3\hat{S}_1$ and $_3\hat{S}_2$ for the local problems $_{12}\mathcal{L}$, $_3\mathcal{I}$ and $_3\mathcal{J}$ respectively, and their nodal displacement relations Eq. (23). In addition, the solution of Eq. (39) is obtained taking into account the corresponding boundary conditions associated to the plane problems $_{12}\mathcal{L}$, $_3\mathcal{I}$ and $_3\mathcal{J}$ according to Table 3.

The completeness of MEE effective moduli is determined substituting the derivates of the prescribed local functions related to the problem $_{12}\mathcal{L}$, $_3\mathcal{I}$ and $_3\mathcal{J}$, as functions of the natural coordinates and the element's shape functions, Eq. (24), into Eqs. (20)–(22). Therefore, the effective properties are calculated by Eq. (40), such as

$$\mathbf{C}^* = \begin{pmatrix} C^*_{1112} & C^*_{2212} & C^*_{3312} & C^*_{1212} & e^*_{312} & q^*_{312}\end{pmatrix}^T, \text{ associated to the local problems }{}_{12}\mathcal{L}, \tag{44}$$

$$\mathbf{C}^* = \begin{pmatrix} e^*_{311} & e^*_{322} & e^*_{333} & e^*_{312} & \kappa^*_{33} & \alpha^*_{33}\end{pmatrix}^T, \text{ associated to the local problems }{}_{3}\mathcal{I}, \tag{45}$$

$$\mathbf{C}^* = \begin{pmatrix} q^*_{311} & q^*_{322} & q^*_{333} & q^*_{312} & \alpha^*_{33} & \mu^*_{33}\end{pmatrix}^T, \text{ associated to the local problems }{}_{3}\mathcal{J}. \tag{46}$$

and $\mathbf{Q}_1$ is the nodal values displacement vector but now associated to these plane problems.

3.3. Analytical approach (AHM)

The analytical solution of the local problems for plane and antiplane states described in compact form (Eqs. (6)–(9)) and the MEE effective moduli (Eqs. (10)–(18)) is obtained. The local problems are solved for a periodic three-phase FRC using complex variable theory combining the complex-potential method, doubly periodic Weierstrass' elliptic functions and so on, see Ref. Guinovart-Díaz et al. (2017).

The antiplane deformation results is studied in Ref. Espinosa-Almeyda et al. (2014) for periodic three-phase FRC with parallelogram cell symmetry and perfect contact. The non-null antiplane effective coefficients formulae for square periodic cell Y are listed as follows

Associated with the local problem $_{\alpha 3}\mathcal{L}$,

$$\begin{aligned} C^*_{\alpha 3\alpha 3} &= C_v + \mathrm{Re}\{\mathrm{Y}_1\,\bar{a}_1 + \mathrm{Y}_2\,\bar{b}_1 + \mathrm{Y}_3\,\bar{e}_1 + \Delta_1\}\delta_{1\alpha} - \mathrm{Im}\{\mathrm{Y}_1\,\bar{a}_1 + \mathrm{Y}_2\,\bar{b}_1 + \mathrm{Y}_3\,\bar{e}_1 - i\Delta_1\}\delta_{2\alpha}, \\ e^*_{\alpha\alpha 3} &= e_v + \mathrm{Re}\{\mathrm{Y}_4\,\bar{a}_1 - \mathrm{Y}_5\,\bar{b}_1 - \mathrm{Y}_6\,\bar{e}_1 + \Delta_2\}\delta_{1\alpha} - \mathrm{Im}\{\mathrm{Y}_4\,\bar{a}_1 - \mathrm{Y}_5\,\bar{b}_1 - \mathrm{Y}_6\,\bar{e}_1 - i\Delta_2\}\delta_{2\alpha}, \\ q^*_{\alpha\alpha 3} &= q_v + \mathrm{Re}\{\mathrm{Y}_7\,\bar{a}_1 - \mathrm{Y}_8\,\bar{b}_1 - \mathrm{Y}_9\,\bar{e}_1 + \Delta_3\}\delta_{1\alpha} - \mathrm{Im}\{\mathrm{Y}_7\,\bar{a}_1 - \mathrm{Y}_8\,\bar{b}_1 - \mathrm{Y}_9\,\bar{e}_1 - i\Delta_3\}\delta_{2\alpha}, \end{aligned} \tag{47}$$

Associated with the local problem ${}_\alpha\mathcal{I}$,

$$\begin{aligned}\kappa^*_{\alpha\alpha} &= \kappa_v + \mathrm{Re}\left\{-\mathrm{Y}_4\,\bar{a}_1 + \mathrm{Y}_5\,\bar{b}_1 + \mathrm{Y}_6\,\bar{e}_1 - \Delta_2\right\}\delta_{1\alpha} - \mathrm{Im}\left\{-\mathrm{Y}_4\,\bar{a}_1 + \mathrm{Y}_5\,\bar{b}_1 + \mathrm{Y}_6\,\bar{e}_1 + i\Delta_2\right\}\delta_{2\alpha},\\ \alpha^*_{\alpha\alpha} &= \alpha_v + \mathrm{Re}\left\{-\mathrm{Y}_7\,\bar{a}_1 + \mathrm{Y}_8\,\bar{b}_1 + \mathrm{Y}_9\,\bar{e}_1 - \Delta_3\right\}\delta_{1\alpha} - \mathrm{Im}\left\{-\mathrm{Y}_7\,\bar{a}_1 + \mathrm{Y}_8\,\bar{b}_1 + \mathrm{Y}_9\,\bar{e}_1 + i\Delta_3\right\}\delta_{2\alpha},\end{aligned} \tag{48}$$

Associated with the local problem ${}_\alpha\mathcal{J}$,

$$\mu^*_{\alpha\alpha} = \mu_v + \mathrm{Re}\left\{-\mathrm{Y}_7\,\bar{a}_1 + \mathrm{Y}_8\,\bar{b}_1 + \mathrm{Y}_9\,\bar{e}_1 - \Delta_3\right\}\delta_{1\alpha} - \mathrm{Im}\left\{-\mathrm{Y}_7\,\bar{a}_1 + \mathrm{Y}_8\,\bar{b}_1 + \mathrm{Y}_9\,\bar{e}_1 + i\Delta_3\right\}\delta_{2\alpha}, \tag{49}$$

where $\tilde{C}_v = \langle C_{\alpha3\alpha3}\rangle / C^{(1)}_{\alpha3\alpha3}$, $e_v = \langle e_{\alpha\alpha3}\rangle / \sqrt{C^{(1)}_{\alpha3\alpha3}\,\kappa^{(1)}_{\alpha\alpha}}$, $q_v = \langle q_{\alpha\alpha3}\rangle / \sqrt{C^{(1)}_{\alpha3\alpha3}\,\mu^{(1)}_{\alpha\alpha}}$, $\kappa_v = \langle\kappa_{\alpha\alpha}\rangle / \kappa^{(1)}_{\alpha\alpha}$, $\alpha_v = \langle\alpha_{\alpha\alpha}\rangle / \sqrt{\kappa^{(1)}_{\alpha\alpha}\,\mu^{(1)}_{\alpha\alpha}}$ and $\mu_v = \langle\mu_{\alpha\alpha}\rangle / \mu^{(1)}_{\alpha\alpha}$ $(\alpha = 1, 2)$. In addition, $\langle f\rangle$ refers to the Voigt average of the relevant quantity f. The remaining coefficients Y_m $(m = 1, \cdots, 9)$ and Δ_i are reported in Appendix D of Ref. Espinosa-Almeyda et al. (2014). Herein, we recall the antiplane effective properties formulae, Eqs. (47)–(49) to check the numerical accuracy of the SAFEM model.

The unknown conjugate complex numbers $\bar{a}_1$, $\bar{b}_1$, and $\bar{e}_1$ are needed for each local problem. They can be found by means of different truncate order N_0 of the following system

$$X = \left[\left(\tilde{E}_1 + R_1^2\tilde{J}\right) - W_{k1}\left(\tilde{E}_p + W_{kp}\right)^{-1} W_{1p}\right]^{-1}\tilde{T}, \tag{50}$$

which is in correspondence with the local problem to be determined. In Eq. (50), the system's solution is represented by $X = (x_1,\ y_1,\ z_1, t_1,\ l_1,\ m_1,\ \ldots, x_k,\ y_k,\ z_k, t_k,\ l_k,\ m_k,\ \ldots)^{\mathrm{T}}$ and the transpose vector of $\tilde{T}$ is $\tilde{T}^{\mathrm{T}} = (\tilde{T}_{11}\delta_{\alpha1},\ \tilde{T}_{11}\delta_{\alpha2},\ \tilde{T}_{21}\delta_{\alpha1},\ \tilde{T}_{21}\delta_{\alpha2},\ \tilde{T}_{31}\delta_{\alpha1},\ \tilde{T}_{31}\delta_{\alpha2}, 0,\ 0,\ 0, 0,\ 0,\ 0,\ \ldots)$. The matrices $\tilde{J}$, $\tilde{E}_p$, and W_{kp} involve in Eq. (50) and the components $\tilde{T}$ are summarized in Appendices B and C of Ref. Espinosa-Almeyda et al. (2014). Details of the construction of the systems and their solution can be seen in Refs. Espinosa-Almeyda et al. (2014), Guinovart-Díaz et al. (2011), and it is omitted here.

In general, the system, Eq. (50), can be solved for a_1, b_1 and e_1, having that $a_1 = x_1 + iy_1$, $b_1 = z_1 + it_1$ and $e_1 = l_1 + im_1$. For the particular case $N_0 = 1$, we have:

$$\begin{pmatrix} a_1 & b_1 & e_1\end{pmatrix}^{\mathrm{T}} = \tilde{Z}\left[\left(\tilde{E}_1 + R_1^2\tilde{J}\right) - W_{k1}\left(\tilde{E}_p + W_{kp}\right)^{-1} W_{1p}\right]^{-1}\tilde{T}_1, \tag{51}$$

where $\tilde{T}_1^{\mathrm{T}} = (\ \tilde{T}_{11}\delta_{\alpha1}\quad \tilde{T}_{11}\delta_{\alpha2}\quad \tilde{T}_{21}\delta_{\alpha1}\quad \tilde{T}_{21}\delta_{\alpha2}\quad \tilde{T}_{31}\delta_{\alpha1}\quad \tilde{T}_{31}\delta_{\alpha2}\ )$ and $\tilde{Z} = \begin{pmatrix} 1 & i & 0 & 0 & 0 & 0\\ 0 & 0 & 1 & i & 0 & 0\\ 0 & 0 & 0 & 0 & 1 & i\end{pmatrix}$.

The plane local problems and effective properties for periodic three-phase FRC with only square and hexagonal cells symmetry and perfect bonding were examined in Refs. Guinovart-Díaz et al. (2013).

The non-null plane effective coefficients formulae for square periodic cell Y are listed as follows:

Elastic:

$$\begin{aligned}&\left(C^*_{1111} + C^*_{1122}\right)/2 = \langle(C_{1111} + C_{1122})/2\rangle - (\mathrm{V}_2 + \mathrm{V}_3)[[(C_{1111} + C_{1122})/2]]_1^2 K_1/C^{(1)}_{1212} -\\ &\mathrm{V}_3[[(C_{1111} + C_{1122})/2]]_1[[(C_{1111} + C_{1122})/2]]_2 K_2/C^{(2)}_{1212} -\\ &\mathrm{V}_3[[(C_{1111} + C_{1122})/2]]_1[[(C_{1111} + C_{1122})/2]]_2 K_3/C^{(1)}_{1212} - \mathrm{V}_3[[(C_{1111} + C_{1122})/2]]_2^2 K_4/C^{(2)}_{1212}\end{aligned}, \tag{52}$$

$$\begin{aligned}&C^*_{1133} = \langle C_{1133}\rangle - (\mathrm{V}_2 + \mathrm{V}_3)[[(C_{1111} + C_{1122})/2]]_1[[C_{1133}]]_1 K_1/C^{(1)}_{1212} -\\ &\mathrm{V}_3[[(C_{1111} + C_{1122})/2]]_1[[C_{1133}]]_2 K_2/C^{(2)}_{1212} - \mathrm{V}_3[[C_{1133}]]_1[[(C_{1111} + C_{1122})/2]]_2 K_3/C^{(1)}_{1212} -,\\ &\mathrm{V}_3[[(C_{1111} + C_{1122})/2]]_2[[C_{1133}]]_2 K_4/C^{(2)}_{1212}\end{aligned} \tag{53}$$

$$\begin{aligned}&C^*_{3333} = \langle C_{3333}\rangle - (\mathrm{V}_2 + \mathrm{V}_3)[[C_{1133}]]_1^2 K_1/C^{(1)}_{1212} - \mathrm{V}_3[[C_{1133}]]_1[[C_{1133}]]_2 K_2/C^{(2)}_{1212} -\\ &\mathrm{V}_3[[C_{1133}]]_1[[C_{1133}]]_2 K_3/C^{(1)}_{1212} - \mathrm{V}_3[[C_{1133}]]_2^2 K_4/C^{(2)}_{1212}\end{aligned}, \tag{54}$$

$$\begin{aligned}&C^*_{3333} = \langle C_{3333}\rangle - (\mathrm{V}_2 + \mathrm{V}_3)[[C_{1133}]]_1^2 K_1/C^{(1)}_{1212} - \mathrm{V}_3[[C_{1133}]]_1[[C_{1133}]]_2 K_2/C^{(2)}_{1212} -\\ &\mathrm{V}_3[[C_{1133}]]_1[[C_{1133}]]_2 K_3/C^{(1)}_{1212} - \mathrm{V}_3[[C_{1133}]]_2^2 K_4/C^{(2)}_{1212}\end{aligned}, \tag{55}$$

$$(C^*_{1111} - C^*_{1122})/2 = \langle C_{1212}\rangle - (\mathrm{V}_2 + \mathrm{V}_3)[[C_{1212}]]_1 M^+ + \mathrm{V}_3[[C_{1212}]]_2, \tag{56}$$

Piezoelectric:

$$\begin{aligned}&e^*_{311} = \langle e_{311}\rangle - (\mathrm{V}_2 + \mathrm{V}_3)[[(C_{1111} + C_{1122})/2]]_1[[e_{311}]]_1 K_1/C^{(1)}_{1212} -\\ &\mathrm{V}_3[[(C_{1111} + C_{1122})/2]]_1[[e_{311}]]_2 K_2/C^{(2)}_{1212} - \mathrm{V}_3[[e_{311}]]_1[[(C_{1111} + C_{1122})/2]]_2 K_3/C^{(1)}_{1212} -,\\ &\mathrm{V}_3[[(C_{1111} + C_{1122})/2]]_2[[e_{311}]]_2 K_4/C^{(2)}_{1212}\end{aligned} \tag{57}$$

$$\begin{aligned}e^*_{333} = \langle e_{333}\rangle &- (\mathrm{V}_2 + \mathrm{V}_3)[[C_{1133}]]_1[[e_{311}]]_1 K_1/C^{(1)}_{1212} - \mathrm{V}_3[[C_{1133}]]_1[[e_{311}]]_2 K_2/C^{(2)}_{1212} -\\ &-\mathrm{V}_3\,[[e_{311}]]_1[[C_{1133}]]_2 K_3/C^{(1)}_{1212} - \mathrm{V}_3[[C_{1133}]]_2[[e_{311}]]_2 K_4/C^{(2)}_{1212},\end{aligned} \tag{58}$$

Table 4
Properties of the materials constituents.

Materials phases	$C_{1111}^{(\gamma)}$ (GPa)	$C_{1122}^{(\gamma)}$ (GPa)	$C_{1133}^{(\gamma)}$ (GPa)	$C_{3333}^{(\gamma)}$ (GPa)	$C_{1313}^{(\gamma)}$ (GPa)
$BaTiO_3$ (BTO)	166	77	78	162	43
$CoFe_2O_4$ (CFO)	286	173	170.5	269.5	45.3
Terfenol D (TD)	31.1	15.2	15.2	35.6	13.6
	$e_{311}^{(\gamma)}$ (C/m^2)	$e_{333}^{(\gamma)}$ (C/m^2)	$e_{113}^{(\gamma)}$ (C/m^2)	$\kappa_{11}^{(\gamma)}$ (C^2/Nm^2)	$\kappa_{33}^{(\gamma)}$ (C^2/Nm^2)
$BaTiO_3$ (BTO)	−4.4	18.6	11.6	11.2×10^{-9}	12.6×10^{-9}
$CoFe_2O_4$ (CFO)	0	0	0	0.08×10^{-9}	0.093×10^{-9}
Terfenol D (TD)	0	0	0	0.05×10^{-9}	0.05×10^{-9}
	$q_{311}^{(\gamma)}$ (N/Am)	$q_{333}^{(\gamma)}$ (N/Am)	$q_{113}^{(\gamma)}$ (N/Am)	$\mu_{11}^{(\gamma)}$ (Ns^2/C^2)	$\mu_{33}^{(\gamma)}$ (Ns^2/C^2)
$BaTiO_3$ (BTO)	0	0	0	5×10^{-6}	10×10^{-6}
$CoFe_2O_4$ (CFO)	580.3	699.7	550	590×10^{-6}	5×10^{-6}
Terfenol D (TD)	156.8	−60.9	108.3	5.4×10^{-6}	5.4×10^{-6}

Piezomagnetic:

$$\begin{aligned} q_{311}^{*} = {} & \langle q_{311}\rangle - (V_2+V_3)[[(C_{1111}+C_{1122})/2]]_1[[q_{311}]]_1K_1/C_{1212}^{(1)} - \\ & V_3[[(C_{1111}+C_{1122})/2]]_1[[q_{311}]]_2K_2/C_{1212}^{(2)} - V_3[[q_{311}]]_1[[(C_{1111}+C_{1122})/2]]_2K_3/C_{1212}^{(1)} -, \\ & V_3[[(C_{1111}+C_{1122})/2]]_2[[q_{311}]]_2K_4/C_{1212}^{(2)} \end{aligned} \tag{59}$$

$$\begin{aligned} q_{333}^{*} = {} & \langle q_{333}\rangle - (V_2+V_3)[[C_{1133}]]_1[[q_{311}]]_1K_1/C_{1212}^{(1)} - V_3[[C_{1133}]]_1[[q_{311}]]_2K_2/C_{1212}^{(2)} - \\ & V_3[[C_{1133}]]_2[[q_{311}]]_1K_3/C_{1212}^{(1)} - V_3[[C_{1133}]]_2[[q_{311}]]_2K_4/C_{1212}^{(2)} \end{aligned}, \tag{60}$$

Dielectric:

$$\begin{aligned} \kappa_{33}^{*} = {} & \langle \kappa_{33}\rangle + (V_2+V_3)[[e_{311}]]_1^2K_1/C_{1212}^{(1)} + V_3[[e_{311}]]_1[[e_{311}]]_2K_2/C_{1212}^{(2)} + \\ & V_3[[e_{311}]]_1[[e_{311}]]_2K_3/C_{1212}^{(1)} + V_3[[e_{311}]]_2^2K_4/C_{1212}^{(2)} \end{aligned}, \tag{61}$$

Magnetoelectric:

$$\begin{aligned} \alpha_{33}^{*} = {} & \langle \alpha_{33}\rangle + (V_2+V_3)[[e_{311}]]_1[[q_{311}]]_1K_1/C_{1212}^{(1)} + V_3[[e_{311}]]_1[[q_{311}]]_2K_2/C_{1212}^{(2)} + \\ & V_3[[q_{311}]]_1[[e_{311}]]_2K_3/C_{1212}^{(1)} + V_3[[e_{311}]]_2[[q_{311}]]_2K_4/C_{1212}^{(2)} \end{aligned}, \tag{62}$$

Magnetic:

$$\begin{aligned} \mu_{33}^{*} = {} & \langle \mu_{33}\rangle + (V_2+V_3)[[q_{311}]]_1^2K_1/C_{1212}^{(1)} + V_3[[q_{311}]]_1[[q_{311}]]_2K_2/C_{1212}^{(2)} + \\ & V_3[[q_{311}]]_1[[q_{311}]]_2K_3/C_{1212}^{(1)} + V_3\|q_{311}\|_2^2K_4/C_{1212}^{(2)} \end{aligned}, \tag{63}$$

and $C_{1212}^{*} = \frac{C_{1111}^{*} - C_{1122}^{*}}{2}$. Herein, $\langle f\rangle$ refers to the Voigt average of f and $[[\,f\,]]_s = f^{(s)} - f^{(s+1)}$ with $s = 1, 2$. The remaining magnitudes K_m $(m = 1, 2, 3, 4)$ and M^{+} are reported Ref. Guinovart-Díaz et al. (2013) and depend on the material constituents of each phase and the composite geometry. Therefore, we have summarized the effective properties formulas to check the numerical accuracy of the SAFEM model through comparison with analytical solutions. Numerical solutions must coincide in order to achieve a good level of validation.

4. Numerical results

The semi-analytical (SAFEM) and analytical (AHM) models reported in the previous sections are applied to study the effect of the interphase thickness and the fiber material properties on the MEE effective properties. Numerical computations for some cases of three-phase (fiber/interphase/matrix) FRC with square periodic cell and different interphase thickness: $t = 0$, 0.01, 0.02, and 0.03 are performed.

First, numerical validation is shown through comparisons between SAFEM and AHM models. They are different mathematical approaches but describing the same physical phenomena, therefore, they must be able to produce similar results. As mentioned before, comparisons between them show the numerical accuracy of SAFEM. As a limit case, a two-phase FRC is also considered when $t = 0$. For this limit case considering a BTO matrix and empty fibers, the numerical values of the herein implemented models reproduce the values reported in Ref. Bravo-Castillero et al. (2009). In general, when considering $t = 0$, the cases of two-phase FRC with perfect interface contact conditions can be reproduced.

The elastic, piezoelectric, dielectric, piezomagnetic, magnetoelectric and magnetic properties used for the numerical calculations are shown in Table 4. The material properties used in the calculations were taken from Ref. Huang and Kuo (1997) for BTO and CFO, and from Ref. Kuo (2011) for Terfenol-D (TD), and $C_{1212}^{(\gamma)} = (C_{1111}^{(\gamma)} - C_{1122}^{(\gamma)})/2$. The Terfenol-D magnetostrictive constituent material is a composite that results from a combination of pure TD with epoxy, therefore, its properties differ to some extent from the properties of pure TD (Branwood, Janio, Piercy, 1987; Giurgiutiu and Lyshevski, 2016; Zhou, Li, Li, & Zhang, 2016).

Table 5
Antiplane MEE effective coefficients obtained by the semi-analytical (SAFEM) and analytical (AHM) present models for a three-phase composite BTO/TD/CFO for different volume fraction of V_2+V_3; and comparison with the models reported by Hashemi (2016), Kuo (2011) and Yan et al. (2013).

V_2+V_3	Models	$C_{1313}^{(\gamma)}$ (GPa)	$e_{113}^{(\gamma)}$ (C/m^2)	$\kappa_{11}^{(\gamma)}\times 10^{-9}$ (C^2/Nm^2)	$q_{113}^{(\gamma)}$ (N/Am)	$\mu_{11}^{(\gamma)}\times 10^{-6}$ (Ns^2/C^2)	$\alpha_{11}^{(\gamma)}\times 10^{-12}$ (Ns/VC)
0.2	SAFEM	42.397	0.016	0.097	389.47	396.141	15.598
	AHM	42.397	0.016	0.097	389.47	396.141	15.598
	Hashemi (2016)	42.1	0.020	0.049	390.6	390.1	15.7
	Kuo (2011)	42.5	0.020	0.049	390.0	390.0	16.0
0.4	SAFEM	39.648	0.035	0.117	271.80	255.280	36.192
	AHM	39.648	0.035	0.117	271.80	255.280	36.192
	Hashemi (2016)	38.93	0.040	0.097	276.4	255.3	36.8
	Kuo (2011)	39.25	0.040	0.098	275.0	255.0	37.5
0.6	SAFEM	37.038	0.058	0.144	176.18	141.247	60.591
	AHM	37.038	0.058	0.144	176.18	141.247	60.591
	Yan et al. (2013)	37.04	0.058	0.1436	176.2	141.2	60.59
	Hashemi (2016)	36.26	0.058	0.144	177.5	140.9	62.1
	Kuo (2011)	37.00	0.0599	0.147	175.0	140.0	63.0

Table 6
Plane MEE effective coefficients obtained by the semi-analytical (SAFEM) and analytical (AHM) present models for a three-phase composite BTO/TD/CFO for different volume fraction of V_2+V_3.

V_2+V_3	Models	C_{1111}^* (GPa)	C_{1122}^* (GPa)	C_{1133}^* (GPa)	C_{3333}^* (GPa)	C_{1212}^* (GPa)	e_{311}^* (C/m^2)
0.2	SAFEM	206.509	112.372	116.443	215.522	45.378	−0.522
	AHM	206.521	112.384	116.453	215.530	45.378	−0.521
0.4	SAFEM	156.289	77.206	83.502	177.837	36.257	−0.839
	AHM	156.514	77.420	83.671	177.968	36.267	−0.838
0.6	SAFEM	119.520	55.369	60.893	148.124	30.135	−1.057
	AHM	120.527	56.373	61.668	148.722	30.143	−1.050
V_2+V_3	Models	e_{333}^* (C/m^2)	q_{311}^* (N/Am)	q_{333}^* (N/Am)	$\kappa_{33}^*\times 10^{-9}$(C^2/Nm^2)	$\alpha_{33}^*\times 10^{-9}$ (Ns/VC)	$\mu_{33}^*\times 10^{-6}$ (Ns^2/C^2)
0.2	SAFEM	2.373	394.008	491.053	1.706	1.164	127.531
	AHM	2.373	394.040	491.078	1.706	1.164	127.531
0.4	SAFEM	4.903	280.486	338.554	3.318	1.787	97.869
	AHM	4.905	281.069	339.004	3.318	1.783	97.867
0.6	SAFEM	7.511	202.568	213.526	4.929	2.145	68.111
	AHM	7.516	205.241	215.589	4.929	2.125	68.104

Table 5 shows a good agreement between SAFEM and AHM. In addition, comparisons with further numerical results reported in the literature are displayed, such as: 1) (Kuo, 2011), which implemented a combination of complex potentials method with a re-expansion formulae and the generalized Rayleigh's formulation to solve the solution of multi-field problem on piezoelectric/piezomagnetic fibrous composites; 2) (Yan et al., 2013), which applied the eigenfunction expansion-variational method to solved the antiplane MEE coupling problem; and 3) (Hashemi, 2016), who developed a micromechanical homogenization scheme to determine the effective moduli of a multiferroic composite with multiphase inhomogeneities.

Tables 5 and 6 illustrate the antiplane and plane MEE effective properties for a three-phase composite BTO/TD/CFO (fiber/interphase/matrix) as a function sum of the interphase and fiber volume fractions (V_2+V_3), which are considered to be equal to 0.2, 0.4 and 0.6. The volume fraction of BTO fiber and its TD interphase satisfies the relation $V_3/V_2=0.5625$, because of $R_2/R_1=0.8$ (Fig. 1). Good concordance among the approaches can be observed.

In addition, the numerical results q_{311}^*, q_{333}^*, μ_{33}^* and α_{33}^* for two and three-phase FRC (BTO/CFO and BTO/PZT-7A/CFO) published in Fig. 2 of Ref. Guinovart-Díaz et al. (2013) can be reproduced by SAFEM herein implemented.

As it has been mentioned since the problem statement, an interphase is considered to describe the contact quality between matrix and fiber, i.e., a three phase composite. The description of the interphase is an open topic that deserves more attention. A multiscale/multiphysics approach must be adequate to proper describe the interphase considering that it can either result from the chemical interactions between constituents or intentionally introduced. For example, the same continuous approach can be applied to nanoscale; in particular, the presented effective moduli can consider also a uniaxial case which is simpler as it can be reduced to a system of parallel springs in nanoporous rod, as reported by Eremeyev and Morozov (2010). However, such implementations are out of the scope of the micromechanics modeling herein employed.

As a first approximation, in this work, it is proposed that the interphase properties can be estimated by the Voigt average as shown in Table 7. Hodzic et al. investigated the interphase region in polymer/glass composite (Hodzic, Stachurski, & Kim, 2000). Theocharopoulos et al. reported the elasticity modulus across the interfaces of yttria stabilized zirconia (YTZP)/veneer interface using nanoindentation (Theocharopoulos et al., 2016). For both works, it can be observed that the interphase properties can be described by the Voigt average as herein proposed. Nevertheless, this assumption is not always true as reported by (Kartheek, Vamsi, Ravisankar, Sivaprasad, & Karthikeyan, 2014) who studied Al/Cu interphase. They obtained higher interphase hardness because of the formation of an intermetallic phase of a few tens micrometers. Another reason to find a

Table 7
MEE effective properties as a function of interphase combinations between BTO and CFO with an interphase thickness and BTO volume fraction equals to 0.01 and 0.3, respectively.

Interphase properties	C^*_{1111} (GPa)		C^*_{1122} (GPa)		C^*_{1133} (GPa)	
	SAFEM	AHM	SAFEM	AHM	SAFEM	AHM
0.2BTO+0.8CFO	237.732	237.735	132.502	132.505	132.487	132.489
0.5BTO+0.5CFO	237.053	237.056	131.962	131.964	131.965	131.967
0.8BTO+0.2CFO	236.187	236.191	131.243	131.246	131.286	131.289
Interphase properties	C^*_{3333} (GPa)		C^*_{1313} (GPa)		C^*_{1212} (GPa)	
	SAFEM	AHM	SAFEM	AHM	SAFEM	AHM
0.2BTO+0.8CFO	228.348	228.350	48.221	48.221	52.384	52.385
0.5BTO+0.5CFO	227.734	227.736	48.166	48.166	52.310	52.310
0.8BTO+0.2CFO	226.985	226.988	48.108	48.108	52.230	52.230
Interphase properties	e^*_{113} (C/m^2)		e^*_{311} (C/m^2)		e^*_{333} (C/m^2)	
	SAFEM	AHM	SAFEM	AHM	SAFEM	AHM
0.2BTO+0.8CFO	0.07238	0.07238	−1.8082	−1.8081	5.2501	5.2502
0.5BTO+0.5CFO	0.07242	0.07242	−1.8330	−1.8329	5.3613	5.3614
0.8BTO+0.2CFO	0.07235	0.07235	−1.8653	−1.8652	5.4660	5.4661
Interphase properties	q^*_{113} (N/Am)		q^*_{311} (N/Am)		q^*_{333} (N/Am)	
	SAFEM	AHM	SAFEM	AHM	SAFEM	AHM
0.2BTO+0.8CFO	286.856	286.856	341.824	341.839	433.845	433.858
0.5BTO+0.5CFO	290.686	290.686	338.548	338.564	429.839	429.853
0.8BTO+0.2CFO	294.474	294.474	334.291	334.309	424.994	425.009
Interphase properties	κ^*_{11} (10^{-9} C^2/Nm^2)		κ^*_{33} (10^{-9} C^2/Nm^2)		$-\alpha^*_{11}$ (10^{-12} Ns/VC)	
	SAFEM	AHM	SAFEM	AHM	SAFEM	AHM
0.2BTO+0.8CFO	0.1541	0.1541	3.9136	3.9136	3.7277	3.7276
0.5BTO+0.5CFO	0.1540	0.1540	3.9876	3.9876	3.6708	3.6708
0.8BTO+0.2CFO	0.1539	0.1539	4.0619	4.0619	3.6143	3.6143
Interphase properties	α^*_{33} (10^{-9} Ns/VC)		μ^*_{11} (10^{-6} Ns^2/C^2)		μ^*_{33} (10^{-6} Ns^2/C^2)	
	SAFEM	AHM	SAFEM	AHM	SAFEM	AHM
0.2BTO+0.8CFO	2.5298	2.5292	309.960	309.961	112.654	112.654
0.5BTO+0.5CFO	2.5234	2.5227	314.035	314.035	111.783	111.783
0.8BTO+0.2CFO	2.5569	2.5561	318.065	318.065	110.917	110.917

deviation from the herein assumption is the rise of residual stresses at the interphase as reported by (Zhang, Allahkarami, & Hanan, 2012) for a zirconia-porcelain interface.

In Table 7, it is shown the effect of interphase properties on the MEE composite moduli. Herein, the effective properties are calculated for a three-phase FRC with CFO matrix, BTO fiber and three combinations for the interphase: 0.2BTO+0.8CFO, 0.5BTO+0.5CFO and 0.8BTO+0.2CFO, having an interphase thickness and BTO volume fraction equals to 0.01 and 0.3, respectively. As can be seen, the effective properties e^*_{311}, e^*_{333}, q^*_{113}, q^*_{311}, q^*_{333}, κ^*_{33}, α^*_{11}, α^*_{33}, μ^*_{11} and μ^*_{33} are more sensitive to the interphase properties than rest ones. These results are predicted by both SAFEM and AHM approaches with a good concordance between them.

In Figs. 3–8, the variations of the non-null effective properties are reported. Also, the effect of the interaction of piezoelectric and piezomagnetic phases in the effective properties is observed. They are calculated for two combinations of three-phase FRC with square periodic cell considering four interphase thicknesses. Figs. 3–5 show the MEE effective moduli versus the BTO (piezoelectric phase) fiber volume fraction and Figs. 6–8 illustrates the same effective moduli versus the CFO (piezomagnetic phase) fiber volume fraction. Here, the MEE coefficients are analyzed up to the maximum admissible fiber volume fraction value for each interphase thickness. The connecting relations among the fiber and interphase volume fractions with the corresponding radii can be written as $V_3 = \pi R_2^2/V$ and $V_2 = \pi[(R_2+t)^2 - R_2^2]/V$ where V is the total volume of Y. In accordance with this last relation, the interphase is considered to grow in the direction toward the matrix, i.e., the matrix volume V_1 decreases as the interphase thickness grows, then $V_1 = 1 - V_2 - V_3$. The possible maximum fiber volume fraction, V_3, is around 0.73, 0.7 and 0.64 when the thickness of the interphase t is equal to 0.01, 0.02 and 0.03, respectively. Herein, the interphase material is considered 50% fiber and 50% matrix.

When the CFO piezomagnetic matrix is reinforced with a BTO piezoelectric fiber, the effective properties e^*_{113}, κ^*_{11} (Fig. 3); C^*_{1111}, C^*_{1122}, C^*_{1133}, C^*_{3333}, C^*_{1212} (Fig. 4); e^*_{311}, q^*_{311}, q^*_{333}, and μ^*_{33} (Fig. 5) have an increasing monotonous behavior as BTO fiber volume fraction increases. The effective properties q^*_{113}, μ^*_{11} (Fig. 3); e^*_{333}, and κ^*_{33} (Fig. 5) monotonously decrease. The magnetoelectric coefficient α^*_{33} (Fig. 4) reaches a maximum value and, then, falls until fiber percolation. C^*_{1313} and α^*_{11} must have the same behavior as α^*_{33}, but it cannot be clearly seen because fiber percolation and the fiber volume for C^*_{1313} and α^*_{11} maximums are quite close. This effect is due to the contribution of the constituent's property of the BTO fiber in the MEE composite. The effective properties C^*_{1313}, e^*_{113}, κ^*_{11}, α^*_{11}, C^*_{1111}, C^*_{1122}, C^*_{1133}, C^*_{3333}, C^*_{1212}, e^*_{311}, q^*_{311}, q^*_{333} and μ^*_{33} (q^*_{113}, μ^*_{11}, α^*_{33},

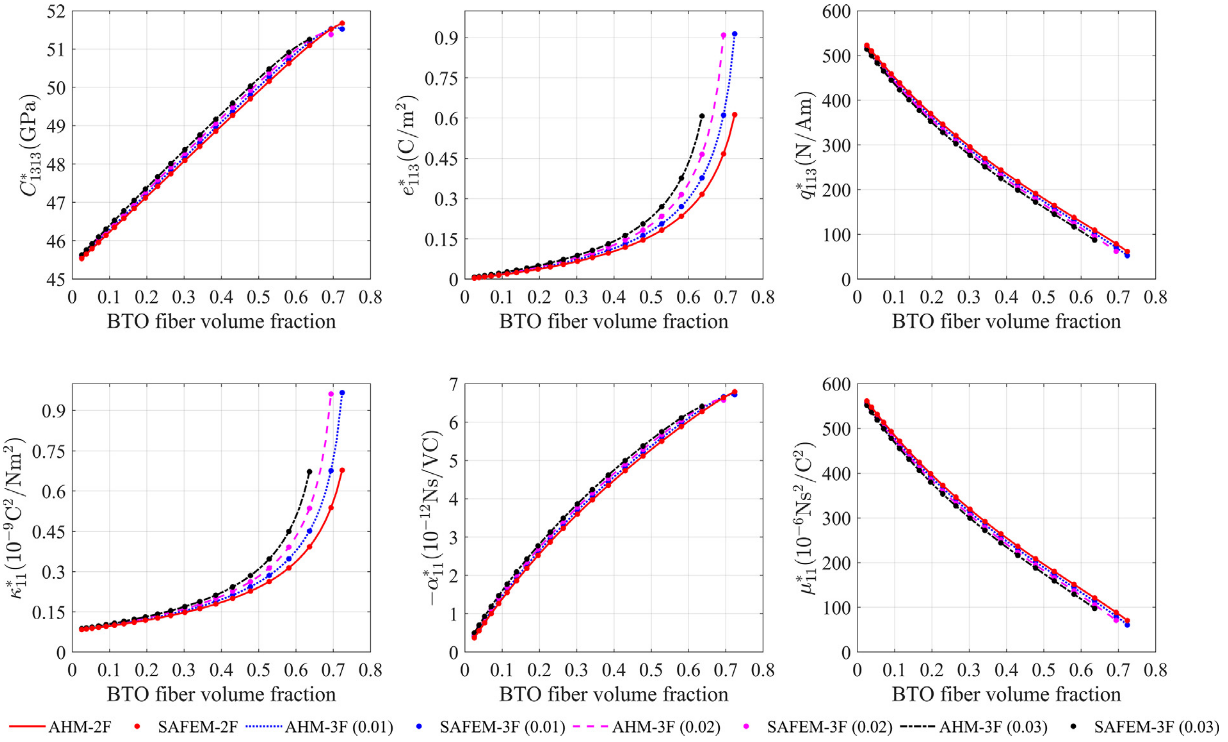

Fig. 3. Variation of the antiplane effective MEE moduli (C^*_{1313}, e^*_{113}, q^*_{113}, κ^*_{11}, α^*_{11} and μ^*_{11}) of a three-phase FRC (CFO piezomagnetic matrix reinforced with BTO piezoelectric fibers) versus fiber volume fraction for different interphase thickness with square periodic cell.

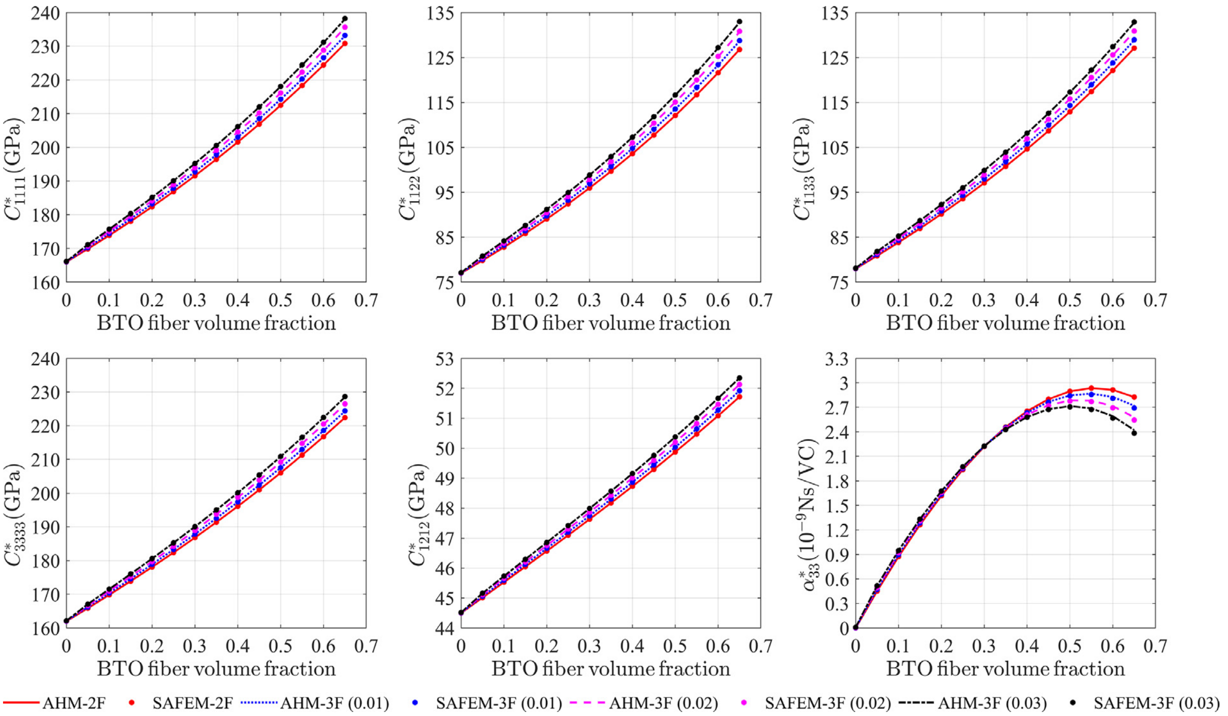

Fig. 4. Variation of the plane effective MEE moduli (C^*_{1111}, C^*_{1122}, C^*_{1133}, C^*_{3333}, C^*_{1212} and α^*_{33}) of a three-phase FRC (CFO piezomagnetic matrix reinforced with BTO piezoelectric fibers) versus fiber volume fraction for different interphase thickness with square periodic cell.

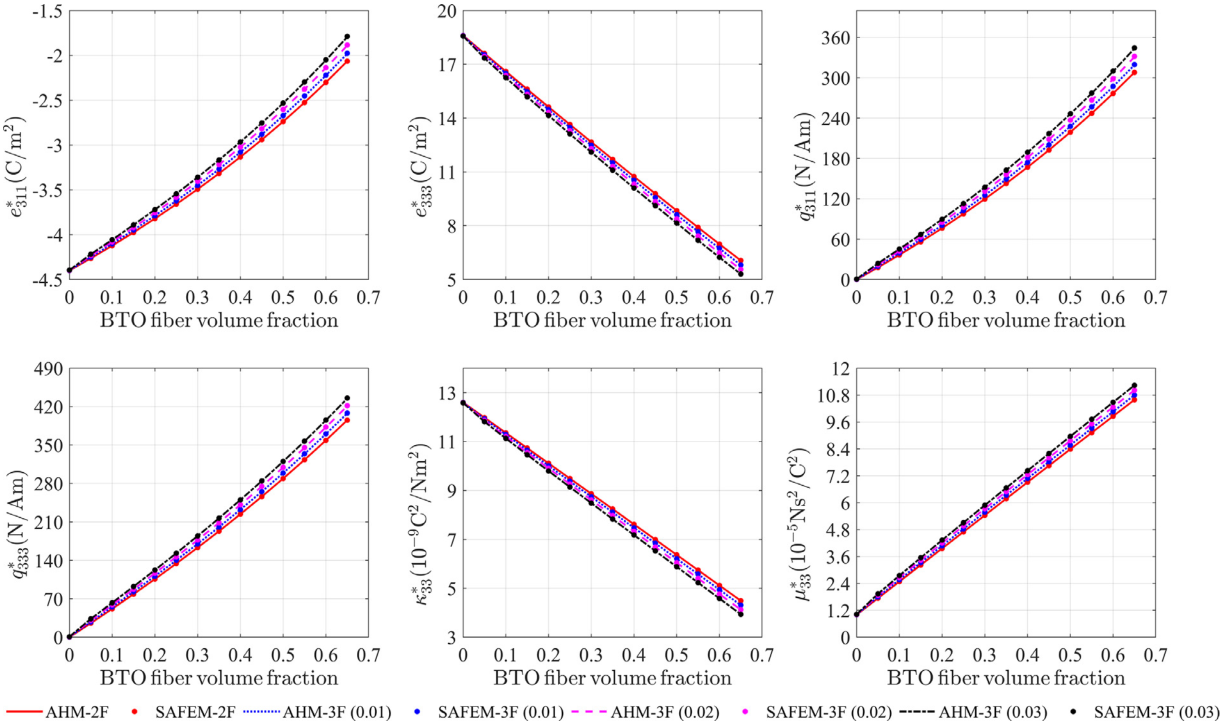

Fig. 5. Variation of the plane effective MEE moduli (e^*_{311}, e^*_{333}, q^*_{311}, q^*_{333}, κ^*_{33} and μ^*_{33}) of a three-phase RFC (CFO piezomagnetic matrix reinforced with BTO piezoelectric fibers) versus fiber volume fraction for different interphase thickness with square periodic cell.

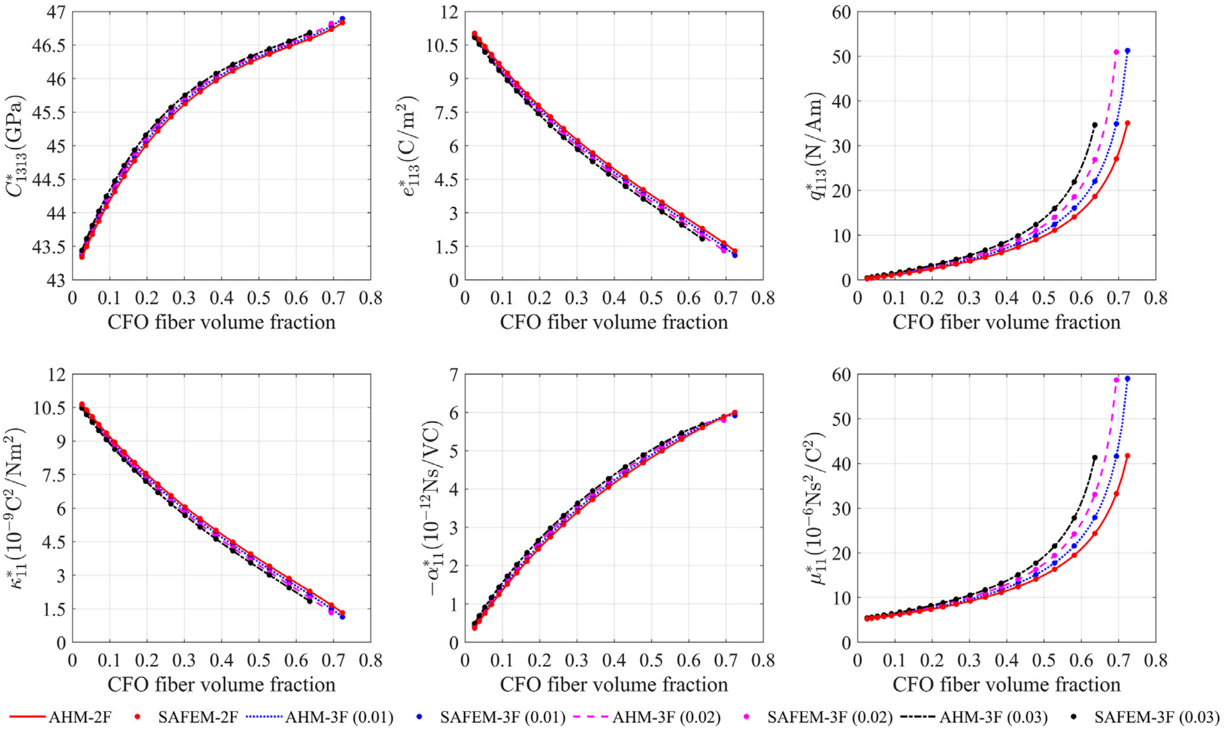

Fig. 6. Variation of the antiplane effective MEE moduli (C^*_{1313}, e^*_{113}, q^*_{113}, κ^*_{11}, α^*_{11} and μ^*_{11}) of a three-phase FRC (BTO piezoelectric matrix reinforced with CFO piezomagnetic fibers) versus fiber volume fraction for different interphase thickness with square periodic cell.

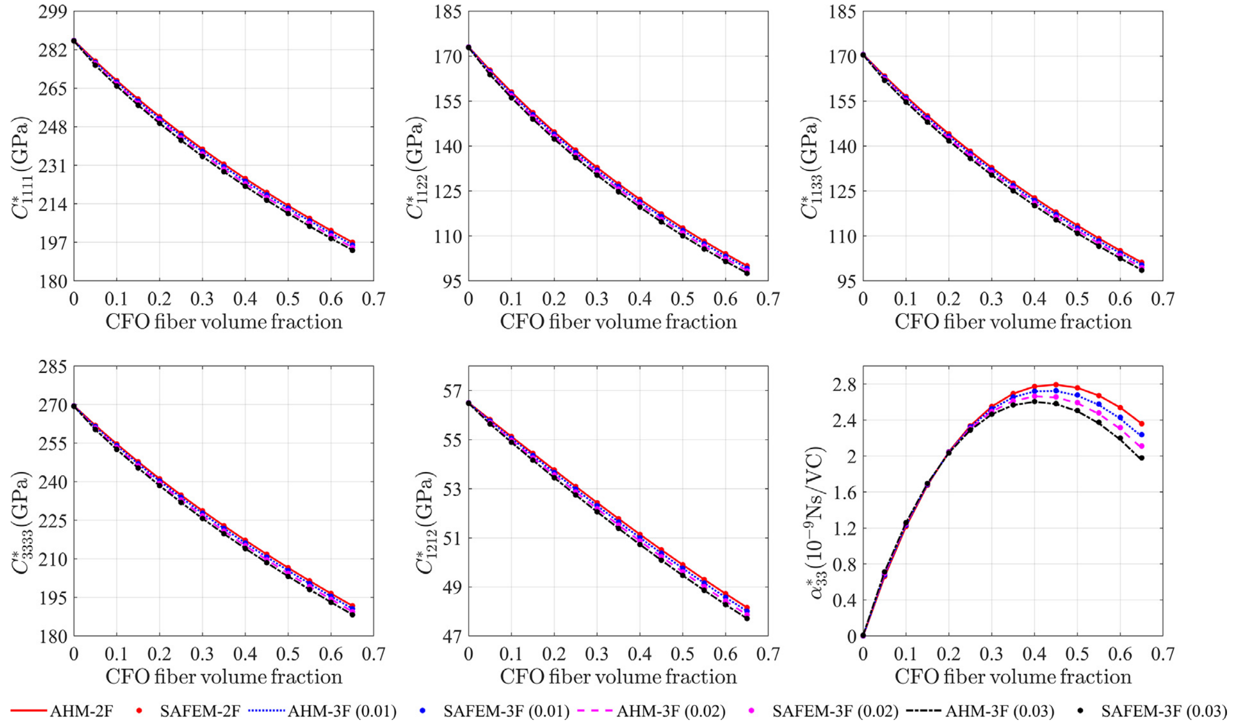

Fig. 7. Variation of the plane effective MEE moduli (C^*_{1111}, C^*_{1122}, C^*_{1133}, C^*_{3333}, C^*_{1212} and α^*_{33}) of a three-phase FRC (BTO piezoelectric matrix reinforced with CFO piezomagnetic fibers) versus fiber volume fraction for different interphase thickness with square periodic cell.

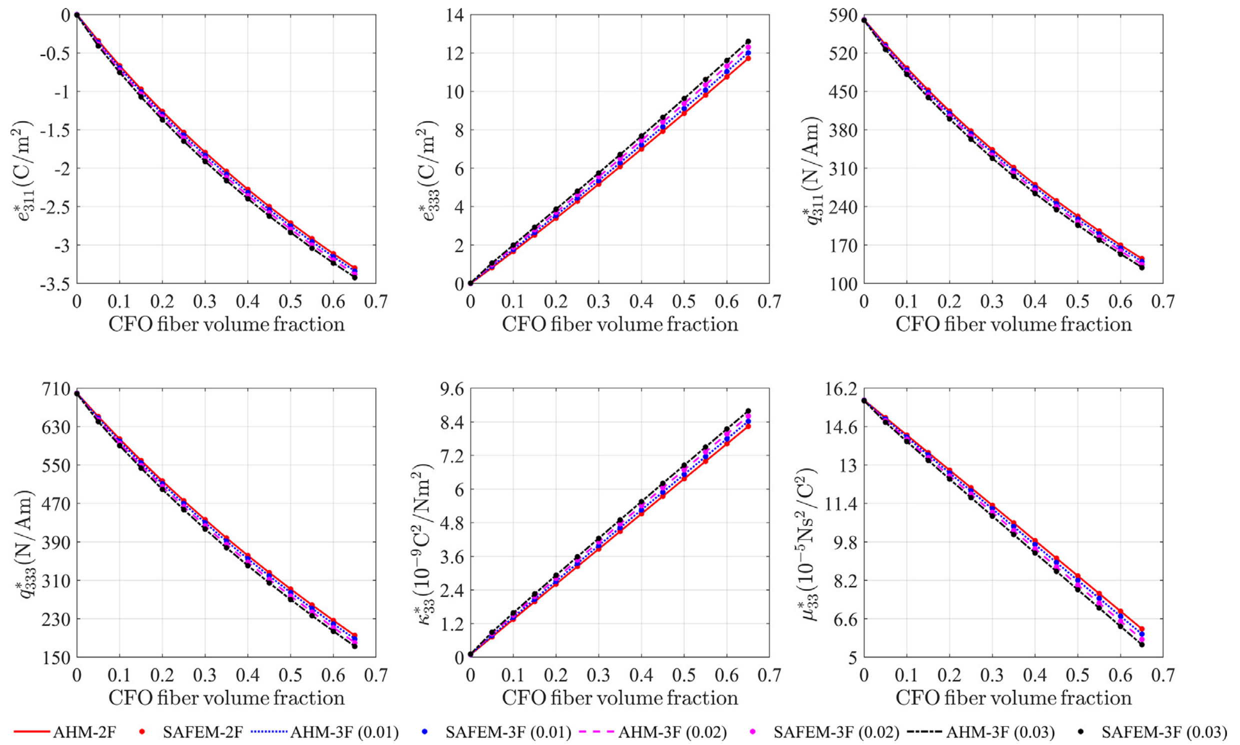

Fig. 8. Variation of the plane effective MEE moduli (e^*_{311}, e^*_{333}, q^*_{311}, q^*_{333}, κ^*_{33} and μ^*_{33}) of a three-phase FRC (BTO piezoelectric matrix reinforced with CFO piezomagnetic fibers) versus fiber volume fraction for different interphase thickness with square periodic cell.

Table 8
MEE effective moduli as a function of interphase volume fraction (V_2) for a three-phase FRC (BTO/TD/CFO) with fiber to matrix volume fraction ratio (V_3/V_1) equal to 0.5625.

V_2	C^*_{1111} (GPa)		C^*_{1122} (GPa)		C^*_{1133} (GPa)	
	SAFEM	AHM	SAFEM	AHM	SAFEM	AHM
0.10	167.6987	167.8915	84.5781	84.7634	89.6016	89.7495
0.15	148.7575	149.0993	72.3776	72.7071	78.4688	78.7285
0.20	133.5134	134.0339	62.9737	63.4786	69.6255	70.0196
0.25	120.7054	121.4337	55.4284	56.1402	62.3002	62.8510
0.30	109.6084	110.5747	49.1992	50.1515	56.0474	56.7789
V_2	C^*_{3333} (GPa)		C^*_{1313} (GPa)		C^*_{1212} (GPa)	
	SAFEM	AHM	SAFEM	AHM	SAFEM	AHM
0.10	184.8275	184.9433	42.3078	42.3078	39.4366	39.4434
0.15	171.5593	171.7603	39.6609	39.6609	35.2265	35.2399
0.20	159.9062	160.2091	37.2516	37.2517	31.6133	31.6351
0.25	149.3268	149.7482	35.0323	35.0324	28.4652	28.4960
0.30	139.5079	140.0657	32.9681	32.9684	25.7073	25.7465
V_2	e^*_{113} (C/m^2)		e^*_{311} (C/m^2)		e^*_{333} (C/m^2)	
	SAFEM	AHM	SAFEM	AHM	SAFEM	AHM
0.10	0.0553	0.0553	−1.2189	−1.2167	6.1003	6.1021
0.15	0.0455	0.0455	−0.9892	−0.9864	5.8752	5.8773
0.20	0.0379	0.0379	−0.8198	−0.8166	5.6077	5.6101
0.25	0.0319	0.0319	−0.6889	−0.6854	5.3132	5.3158
0.30	0.0269	0.0269	−0.5842	−0.5805	5.0003	5.0032
V_2	q^*_{113} (N/Am)		q^*_{311} (N/Am)		q^*_{333} (N/Am)	
	SAFEM	AHM	SAFEM	AHM	SAFEM	AHM
0.10	247.9972	248.0028	268.8079	269.3775	330.3145	330.7604
0.15	240.7217	240.7220	255.5824	256.4988	303.4858	304.1949
0.20	232.7185	232.7407	244.0937	245.4071	277.9043	278.9137
0.25	224.1693	224.2116	233.8757	235.6393	253.2393	254.5885
0.30	215.1892	215.2681	224.6347	226.9078	229.2814	231.0148
V_2	κ^*_{11} (10^{-9} C^2/Nm^2)		κ^*_{33} (10^{-9} C^2/Nm^2)		$-\alpha^*_{11}$ (10^{-12} Ns/VC)	
	SAFEM	AHM	SAFEM	AHM	SAFEM	AHM
0.10	0.1396	0.1396	4.1729	4.1729	37.5935	37.5958
0.15	0.1290	0.1290	3.9471	3.9471	43.1016	43.1068
0.20	0.1200	0.1200	3.7201	3.7201	45.0768	45.0870
0.25	0.1123	0.1123	3.4923	3.4922	44.8825	44.9011
0.30	0.1054	0.1054	3.2639	3.2639	43.3302	43.6229
V_2	α^*_{33} (10^{-9} Ns/VC)		μ^*_{11} (10^{-6} Ns^2/C^2)		μ^*_{33} (10^{-6} Ns^2/C^2)	
	SAFEM	AHM	SAFEM	AHM	SAFEM	AHM
0.10	2.1837	2.1769	240.5826	240.5892	94.5565	94.5548
0.15	1.9934	1.9858	221.6379	221.6526	89.6121	89.6096
0.20	1.8266	1.8184	203.2118	203.2427	84.6661	84.6627
0.25	1.6755	1.6669	185.2102	185.2735	79.7187	79.7144
0.30	1.5354	1.5265	167.5328	167.6595	74.7702	74.7648

e^*_{333} and κ^*_{33}) increases (decreases) as the interphase thickness increases. This effect is more noticeable for the higher fiber volume fraction, but not for lower values. Also, from Figs. 3 to 5, it can be observed that the numerical results of SAFEM and AHM are in a good concordance.

Let us exchange the materials constituents between the matrix and the fiber, i.e., BTO piezoelectric matrix is now reinforced with a CFO piezomagnetic fiber. As expected, the effective properties monotonous behavior changes with the increase of the CFO volume fraction in comparison with the previous case of BTO fiber (Figs. 3–5), with the exception of C^*_{1313}, α^*_{11} and α^*_{33}, as can be seen in Figs. 6–8. These three effective coefficients have in common that they increase, reach a maximum value and, then, they fall. Now, the effective coefficients e^*_{113}, κ^*_{11}, C^*_{1111}, C^*_{1122}, C^*_{1133}, C^*_{3333}, C^*_{1212}, e^*_{311}, q^*_{311}, q^*_{333}, and μ^*_{33} (q^*_{113}, μ^*_{11}, e^*_{333} and κ^*_{33}) decreases (increases) as the interphase thickness increases. The interphase thickness effect on the effective coefficients C^*_{1313}, α^*_{11} and α^*_{33} is the same one for both matrix and fiber combinations. From Figs. 3 to 8, it is possible to see that the magnetoelectric effective properties α^*_{11} and α^*_{33} arise as consequence of the interaction between piezoelectric and piezomagnetic phases, as it is reported in Ref. Hashemi (2016).

Table 8 reports the MEE effective moduli as a function of interphase (TD) volume fraction (V_2) for a three-phase FRC (BTO/TD/CFO) with fiber to matrix volume fraction ratio (V_3/V_1) equal to 0.5625. It can be observed that, as V_2 increases, all effective properties values decrease with the exception of the magnetoelectric coefficient α^*_{11}. This decrease can be related to the fact that TD has lower constitutive values than those of BTO and CFO and the TD relative volume fraction increment. The observed exception with α^*_{11} seems to be unexpected because of the q^*_{113} lower constituent value for TD. A plausible explanation should be found in the stress field developed during the magnetic-electric field coupling.

Finally, it has been proved that SAFEM is an effective method to calculate the effective properties for a MEE composite and it is also accurate to describe the effect of the interphase. It is also shown that the interface thickness plays an important role on the composite properties.

5. Conclusions

In this work, the implementation of a semi-analytical approach based on the Asymptotic Homogenization (AHM) and Finite Element (FEM) methods is developed for computing the magneto-electro-elastic (MEE) effective moduli of three-phase fiber-reinforced periodic composite. The solution of the antiplane and plane local problems derived from AHM is solved via the principle of minimum potential energy through FEM. The implemented model considers the effect of the interphase thickness between fiber and matrix. The numerical results were verified by means of comparisons between the analytical AHM and SAFEM methods under a variety of cases with special focus on the interphase effect on the composite properties. For all the cases, good coincidences are obtained between both approximations. A comparison with the literature also reports a good agreement. Hence, SAFEM proves to also provide good effective properties estimations. Herein, the influence of the interphase thickness and the constituent properties on the composite effective properties is studied.

Acknowledgments

The author YEA gratefully acknowledges the Program of Postdoctoral Scholarships of DGAPA from UNAM, México. HCM and YEA are grateful to the support of the CONACYT Basic science grant A1-S-9232. The author JAO is grateful to the CONACYT support grant number 253087 for the stay at Autonomous University of Ciudad Juárez. The author FJS is grateful to the support of the project PAPIIT-DGAPA-UNAM IA100919. The author RRR thanks to PREI-DGAPA and Department of Mathematics and Mechanics of IIMAS at UNAM for the facilities and support to his research project.

Appendix A

The vectors and matrices define in Eqs. (33)–(35) related to the antiplane local problems are presented by the form:

$$\mathbf{D}_a = \begin{pmatrix} C_{1313}\delta_{1\alpha} & C_{1313}\delta_{2\alpha} & e_{113}\delta_{1\alpha} & e_{113}\delta_{2\alpha} & q_{113}\delta_{1\alpha} & q_{113}\delta_{2\alpha} \end{pmatrix},$$

$$\mathbf{C}_a = \begin{pmatrix} e_{113}\delta_{1\alpha} & e_{113}\delta_{2\alpha} & -\kappa_{11}\delta_{1\alpha} & -\kappa_{11}\delta_{2\alpha} & -\alpha_{11}\delta_{1\alpha} & -\alpha_{11}\delta_{2\alpha} \end{pmatrix},$$

and

$$\mathbf{G}_a = \begin{pmatrix} q_{113}\delta_{1\alpha} & q_{113}\delta_{2\alpha} & -\alpha_{11}\delta_{1\alpha} & -\alpha_{11}\delta_{2\alpha} & -\mu_{11}\delta_{1\alpha} & -\mu_{11}\delta_{2\alpha} \end{pmatrix} \text{ with } (\alpha = 1,\ 2) \text{ Also.}$$

$$\mathbf{B}_a = \begin{pmatrix} J_{11} & J_{12} & 0 & 0 & 0 & 0 \\ J_{21} & J_{22} & 0 & 0 & 0 & 0 \\ 0 & 0 & J_{11} & J_{12} & 0 & 0 \\ 0 & 0 & J_{21} & J_{22} & 0 & 0 \\ 0 & 0 & 0 & 0 & J_{11} & J_{12} \\ 0 & 0 & 0 & 0 & J_{21} & J_{22} \end{pmatrix}$$
$$\times \begin{pmatrix} \frac{\partial\psi_1}{\partial\zeta_1} & 0 & 0 & \frac{\partial\psi_2}{\partial\zeta_1} & 0 & 0 & \cdots & \frac{\partial\psi_7}{\partial\zeta_1} & 0 & 0 & \frac{\partial\psi_8}{\partial\zeta_1} & 0 & 0 \\ \frac{\partial\psi_1}{\partial\zeta_2} & 0 & 0 & \frac{\partial\psi_2}{\partial\zeta_2} & 0 & 0 & \cdots & \frac{\partial\psi_7}{\partial\zeta_2} & 0 & 0 & \frac{\partial\psi_8}{\partial\zeta_2} & 0 & 0 \\ 0 & \frac{\partial\psi_1}{\partial\zeta_1} & 0 & 0 & \frac{\partial\psi_2}{\partial\zeta_1} & 0 & \cdots & 0 & \frac{\partial\psi_7}{\partial\zeta_1} & 0 & 0 & \frac{\partial\psi_8}{\partial\zeta_1} & 0 \\ 0 & \frac{\partial\psi_1}{\partial\zeta_2} & 0 & 0 & \frac{\partial\psi_2}{\partial\zeta_2} & 0 & \cdots & 0 & \frac{\partial\psi_7}{\partial\zeta_2} & 0 & 0 & \frac{\partial\psi_8}{\partial\zeta_2} & 0 \\ 0 & 0 & \frac{\partial\psi_1}{\partial\zeta_1} & 0 & 0 & \frac{\partial\psi_2}{\partial\zeta_1} & \cdots & 0 & 0 & \frac{\partial\psi_7}{\partial\zeta_1} & 0 & 0 & \frac{\partial\psi_8}{\partial\zeta_1} \\ 0 & 0 & \frac{\partial\psi_1}{\partial\zeta_2} & 0 & 0 & \frac{\partial\psi_2}{\partial\zeta_2} & \cdots & 0 & 0 & \frac{\partial\psi_7}{\partial\zeta_2} & 0 & 0 & \frac{\partial\psi_8}{\partial\zeta_2} \end{pmatrix}.$$

References

Álvarez-Borges, F. E., Bravo-Castillero, J., Cruz, M. E., Guinovart-Díaz, R., Pérez-Fernández, L. D., Rodríguez-Ramos, R., & Sabina, F. J. (2018). Reiterated homogenization of a laminate with imperfect contact: gain-enhancement of effective properties. *Applied Mathematics and Mechanics, 39*, 1119–1146.

Bakhvalov, N. S., & Panasenko, G. P. (1989). *Homogenization averaging processes in periodic media*. Dordrecht: Kluwer Academic.

Barulich, N. D., Godoy, L. A., & Dardati, P. M. (2016). A computational micromechanics approach to evaluate elastic properties of composites with fiber-matrix interface damage. *Composite Structures, 154*, 309–318.

Berger, H., Gabbert, U., Köppe, H., Rodriguez-Ramos, R., Bravo-Castillero, J., Guinovart-Diaz, R., Otero, J. A., & Maugin, G. A. (2003). Finite element and asymptotic homogenization methods applied to smart composite materials. *Computational Mechanics, 33*, 61–67.

Berger, H., Kari, S., Gabbert, U., Rodriguez-Ramos, R., Guinovart, R., Otero, J. A., & Bravo-Castillero, J. (2005). An analytical and numerical approach for calculating effective material coefficients of piezoelectric fiber composites. *International Journal of Solids and Structures, 42*, 5692–5714.

Branwood, A., Janio, A. L., & Piercy, A. R. (1987). Domain structures in polycrystalline Tb0.27Dy0.73Fe2 (Terfenol) in the applied field region of optimum magnetoelastic properties. *Journal of Applied Physics, 61*, 3796–3798.

Bravo-Castillero, J., Rodríguez-Ramos, R., Guinovart-Díaz, R., Sabina, F. J., Aguiar, A. R., Silva, U. P., & Gómez-Muñoz, J. L. (2009). Analytical formulae for electromechanical effective properties of 3–1 longitudinally porous piezoelectric materials. *Acta Materialia, 57*, 795–803.

Camacho-Montes, H., Rodríguez-Ramos, R., Bravo-Castillero, J., Guinovart-Díaz, R., & Sabina, F. J. (2006). Effective coefficients for two phase magneto-electroelastic fibrous composite with square symmetry cell in-plane mechanical displacement and out-of-plane electric and magnetic field case. *Integrated Ferroelectrics, 83*, 49–65.

Camacho-Montes, H., Sabina, F. J., Bravo-Castillero, J., Guinovart-Díaz, R., & Rodríguez-Ramos, R. (2009). Magnetoelectric coupling and cross-property connections in a square array of a binary composite. *International Journal of Engineering Science, 47*, 294–312.

Cheng, Y., Peng, B., Hu, Z., Zhou, Z., & Liu, M. (2018). Recent development and status of magnetoelectric materials and devices. *Physics Letters A, 382*, 3018–3025.

Ciomaga, C. E., Avadanei, O. G., Dumitru, I., Airimioaei, M., Tascu, S., Tufescu, F., & Mitoseriu, L. (2016). Engineering magnetoelectric composites towards application as tunable microwave filters. *Journal of Physics D: Applied Physics, 49*, 125002.

Eremeyev, V. A., & Morozov, N. F. (2010). The effective stiffness of a nanoporous rod. *Doklady Physics, 55*, 279–282.

Espinosa-Almeyda, Y., Camacho-Montes, H., Rodríguez-Ramos, R., Guinovart-Díaz, R., López-Realpozo, J. C., Bravo-Castillero, J., & Sabina, F. J. (2017). Influence of imperfect interface and fiber distribution on the antiplane effective magneto-electro-elastic properties for fiber reinforced composites. *International Journal of Solids and Structures, 112*, 155–168.

Espinosa-Almeyda, Y., Rodríguez-Ramos, R., Guinovart-Díaz, R., Bravo-Castillero, J., López-Realpozo, J. C., Camacho-Montes, H., Sabina, F. J., & Lebon, F. (2014). Antiplane magneto-electro-elastic effective properties of three-phase fiber composites. *International Journal of Solids and Structures, 51*, 3508–3521.

Geng, L. D., Yan, Y., Priya, S., & Wang, Y. U. (2017). Theoretical model and computer simulation of Metglas/PZT magnetoelectric composites for voltage tunable inductor applications. *Acta Materialia, 140*, 97–106.

Giurgiutiu, V., & Lyshevski, S. E. (2016). *Micromechatronics: Modeling, analysis, and design with MATLAB* (2nd ed.). CRC Press.

Guinovart-Díaz, R., López-Realpozo, J. C., Rodríguez-Ramos, R., Bravo-Castillero, J., Ramírez, M., Camacho-Montes, H., & Sabina, F. J. (2011). Influence of parallelogram cells in the axial behaviour of fibrous composite. *International Journal of Engineering Science, 49*, 75–84.

Guinovart-Díaz, R., Rodríguez-Ramos, R., Bravo-Castillero, J., Sabina, F. J., Monsivais Galindo, G., & Wang, Y.-S. (2013). Plane magneto-electro-elastic moduli of fiber composites with interphase. *Mechanics of Advanced Materials and Structures, 20*, 552–563.

Guinovart-Díaz, R., Rodríguez-Ramos, R., Espinosa-Almeyda, Y., López-Realpozo, J. C., Dumont, S., Lebon, F., & Conci, A. (2017). An approach for modeling three-phase piezoelectric composites. *Mathematical Methods in the Applied Sciences, 40*, 3230–3248.

Guinovart-Sanjuán, D., Vajravelu, K., Rodríguez-Ramos, R., Guinovart-Díaz, R., Bravo-Castillero, J., Lebon, F., & Sabina, F. J. (2018). Analysis of effective elastic properties for shell with complex geometrical shapes. *Composite Structures, 203*, 278–285.

Hashemi, R. (2016). Magneto-electro-elastic properties of multiferroic composites containing periodic distribution of general multi-coated inhomogeneities. *International Journal of Engineering Science, 103*, 59–76.

Hodzic, A, Stachurski, Z. H., & Kim, J. K. (2000). Nano-indentation of polymer–glass interfaces Part I. Experimental and mechanical analysis. *Polymer, 41*, 6895–6905. doi:10.1016/S0032-3861(99)00890-3.

Huang, J. H., & Kuo, W.-S. (1997). The analysis of piezoelectric/piezomagnetic composite materials containing ellipsoidal inclusions. *Journal of Applied Physics, 81*, 1378–1386.

Kartheek, S. S. M., Vamsi, K. V., Ravisankar, B., Sivaprasad, K., & Karthikeyan, S. (2014). Microstructural and Nanoindentation Studies Across Diffusion-bonded Interfaces in Al/Cu Metal Intermetallic Laminates. *Procedia Materials Science, 6*, 709–715.

Kosub, T., Kopte, M., Hühne, R., Appel, P., Shields, B., Maletinsky, P., Hübner, R., Liedke, M. O., Fassbender, J., Schmidt, O. G., & Makarov, D. (2017). Purely antiferromagnetic magnetoelectric random access memory. *Nature Communications, 8*, 13985.

Koutsawa, Y., Karatrantos, A., Yu, W., & Ruch, D. (2018). A micromechanics approach for the effective thermal conductivity of composite materials with general linear imperfect interfaces. *Composite Structures, 200*, 747–756.

Kuo, H.-Y. (2011). Multicoated elliptic fibrous composites of piezoelectric and piezomagnetic phases. *International Journal of Engineering Science, 49*, 561–575.

Lebon, F., Dumont, S., Rizzoni, R., López-Realpozo, J. C., Guinovart-Díaz, R., Rodríguez-Ramos, R., Bravo-Castillero, J., & Sabina, F. J. (2016). Soft and hard anisotropic interface in composite materials. *Composites Part B: Engineering, 90*, 58–68.

Lee, H., Lee, A., Wang, S., Ebrahimi, F., Gupta, P., Amiri, P. K., & Wang, K. L. (2017). A word line pulse circuit technique for reliable magnetoelectric random access memory. *IEEE Transactions on Very Large Scale Integration (VLSI) Systems, 25*, 2027–2034.

Lin, H., Lou, J., Gao, Y., Hasegawa, R., Liu, M., Howe, B., Jones, J., Brown, G., & Sun, N. X. (2015). Voltage tunable magnetoelectric inductors with improved operational frequency and quality factor for power electronics. *IEEE Transactions on Magnetics, 51*, 1–5.

Naifar, S., Bradai, S., Viehweger, C., Choura, S., Kanoun, O., 2018. Evaluation of multiple transducers implementation in a magnetoelectric vibration energy harvester, tm - Technisches Messen, p. 580.

Otero, J. A., Rodríguez-Ramos, R., Bravo-Castillero, J., Guinovart-Díaz, R., Sabina, F. J., & Monsivais, G. (2013). Semi-analytical method for computing effective properties in elastic composite under imperfect contact. *International Journal of Solids and Structures, 50*, 609–622.

Otero, J. A., Rodríguez-Ramos, R., & Monsivais, G. (2016). Computation of effective properties in elastic composites under imperfect contact with different inclusion shapes. *Mathematical Methods in the Applied Sciences, 40*, 3290–3310.

Pobedrya, B. E. (1984). *Mechanics of composite materials*. Moscow State University Press (in Russian).

Popov, M. A., Zavislyak, I. V., & Srinivasan, G. (2018). Current tunable barium hexaferrite millimeter wave resonator. *Microwave and Optical Technology Letters, 60*, 458–462.

Qiu, J., Chen, H., Wen, Y., & Li, P. (2015). Magnetoelectric and electromagnetic composite vibration energy harvester for wireless sensor networks. *Journal of Applied Physics, 117*, 17A331.

Qiu, J., Tang, X., Chen, H., Liu, X., & Hu, Z. (2017). A tunable broadband magnetoelectric and electromagnetic hybrid vibration energy harvester based on nanocrystalline soft magnetic film. *Surface and Coatings Technology, 320*, 447–451.

Reis, S., Castro, N., Silva, M. P., Correia, V., Rocha, J. G., Martins, P., & Lanceros-Mendez, S. (2017). Fabrication and characterization of high-performance polymer-based magnetoelectric DC magnetic field sensors devices. *IEEE Transactions on Industrial Electronics, 64*, 4928–4934.

Sixto-Camacho, L. M., Bravo-Castillero, J., Brenner, R., Guinovart-Díaz, R., Mechkour, H., Rodríguez-Ramos, R., & Sabina, F. J. (2013). Asymptotic homogenization of periodic thermo-magneto-electro-elastic heterogeneous media. *Computers & Mathematics with Applications, 66*, 2056–2074.

Theocharopoulos, A. A.-O., Bushby, A. J., P'Ng K, M., Wilson, R. M., Tanner, K. A.-O., & Cattell, M. A.-O. (2016). Interfacial modulus mapping of layered dental ceramics using nanoindentation. *J Adv Prosthodont, 8*, 479–488.

Wang, Y., Xia, X. D., & Weng, G. J. (2017). Magnetoelectric coupling and interface effects of multiferroic composites under strees-prescribed boundary condition. *Reviews on Advanced Materials Science, 48*, 78–90.
Yan, P., Jiang, C. P., & Song, F. (2013). Unified series solution for the anti-plane effective magnetoelectroelastic moduli of three-phase fiber composites. *International Journal of Solids and Structures, 50*, 176–185.
Zhang, Y, Allahkarami , M, & Hanan, J. C. (2012). Measuring residual stress in ceramic zirconia-porcelain dental crowns by nanoindentation. *J Mech Behav Biomed Mater, 6*, 120–127. doi:10.1016/j.jmbbm.2011.11.006.
Zhou, H.-M., Li, M.-H., Li, X.-H., & Zhang, D.-G. (2016). An analytical and explicit multi-field coupled nonlinear constitutive model for Terfenol-D giant magnetostrictive material. *Smart Materials and Structures, 25*, 085036.
Zienkiewicz, O. C., Taylor, R. L., & Zhu, J. Z. (2013). *The finite element method: Its basis and fundamentals* (7th ed.). Butterworth-Heinemann.